

Fatigue Damage In Titanium Graphite Hybrid Laminates

by

Dennis Arthur Burianek

S.B., Massachusetts Institute of Technology
(1996)

Submitted to the Department of Aeronautics and Astronautics
in partial fulfillment of the requirements for the degree of

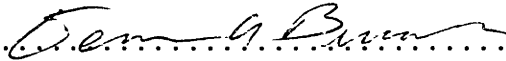
Master of Science in Aeronautics and Astronautics


at the

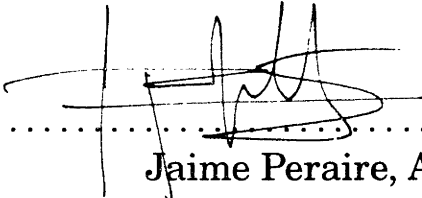
MASSACHUSETTS INSTITUTE OF TECHNOLOGY

February 1998

© Massachusetts Institute of Technology 1998. All rights reserved.

Author.....
Department of Aeronautics and Astronautics
January 12, 1998

Certified by.....
S. Mark Spearing
Assistant Professor of Aeronautics and Astronautics
Thesis Supervisor

Accepted by.....
Jaime Peraire, Associate Professor
Chairman, Department Committee on Graduate Students

MASSACHUSETTS INSTITUTE OF TECHNOLOGY

ARCHIVE

MAR 09 1998

Acknowledgments

The completion of this work would not have been possible without the tremendous support I have received from my co-workers and friends. I would like to thank my advisor, Mark Spearing, who's hard work and helpful advice made this whole project possible.

In addition, the HSCT Structures group at The Boeing Company (Ron Zabora, Bill Westre, Antonio Rufin, Ed Li, Mathew Miller, Ted Reinhardt and many others) provided me with a wealth of material necessary to perform the experiments.

I would also like to thank the staff and faculty of TELAC and the Aero/Astro Dept. for supporting my efforts. Paul, Hugh, and Carlos for asking questions that made me think about the problems at hand. Plus the other graduate students in TELAC for helping me learn the ropes of being a grad student, especially Staci for proofreading the final draft of this report. and Ping and Deb for their support. A special thanks goes to John Kane for always being available to help me in the lab and to Don Weiner and Dick Perdichizzi for help in the machine shop. Without Dick's innovative idea, the stiffness measurements might not have worked. The three undergrads who have helped me in the lab, Todd, Barbara, and Julio, gave me enormous amounts of help and made sure nothing blew up on me.

The key people in keeping me sane outside the lab (and sometimes in the lab) have been the friends I have made since coming to MIT. Shawn, Luis, Brian (who says without his help I would be living in a box playing with paper airplanes), Malinda, Jean, Anand, Eric, Vicki, and especially Sarah.

And last, but not least, the most important people in getting me through MIT and life in general have been my family. My parents have always supported me in whatever I was doing and my two brothers, Joe and Mike and their families and my sister, Theresa, have always helped me through the tough decisions of life. Without my family, I wouldn't be where I am today.

This research was funded by The Boeing Company under purchase order numbers: TO 523782 07LLN for 1997 and FO 563287 07LLN for 1996.

Contents

1	Introduction	11
1.1	Hybrid Laminates	11
1.2	Objectives	12
2	Background	14
2.1	Overview of Hybrid Laminates	14
2.1.1	ARALL and GLARE	14
2.1.2	TiGr	17
2.2	Fatigue of Metals	18
2.3	Fatigue Effects in Polymer Matrix Composites	20
2.4	Summary	21
3	Experimental Procedure	22
3.1	Test Specimens	22
3.2	Test Equipment	24
3.2.1	Load frame	24
3.2.2	Temperature cabinet	24
3.2.3	Anti-buckling guide	27
3.2.4	Extensometer	34
3.3	Test Procedure	37
3.3.1	Specimen preparation	39
3.3.2	Fatigue test procedure	39
3.4	Polishing and Microscopy	44

4	Experimental Results	46
4.1	Open Hole Tension Tests	46
4.2	Damage Progression	47
4.2.1	Damage modes	48
4.2.2	Damage mapping	52
4.3	Fatigue Tests	58
4.3.1	Failure mechanisms	58
4.3.2	Fatigue life results	62
4.3.3	Residual strength tests	62
4.4	Room temperature test	65
4.5	Summary	66
5	Discussion	67
5.1	Facesheet Cracking	67
5.1.1	Stress concentration	68
5.1.2	Titanium fatigue cracks	68
5.1.3	Crack growth	74
5.2	0° Ply Splitting	75
5.3	Strain Energy Release Rate	78
5.4	Stiffness Reduction	80
5.5	Damage Growth Correlation	86
5.6	Residual Strength	86
5.7	Design Implications	88
5.7.1	Stress concentration factor	88
5.7.2	Strain energy release rate	90
6	Conclusions	92
6.1	Project Summary	92
6.2	Recommendations for Future Study	93
	References	94

Appendix A	99
A.1 Stress Concentration Code	99
A.2 Strain Energy Release Rate Code	102
A.3 Stiffness Loss Code	103

List of Figures

1-1	TiGr laminate	12
3-1	Test specimens	23
3-2	Load frame and controller	25
3-3	Temperature cabinet	26
3-4	Cabinet set-up	27
3-5	Thermocouple placement	28
3-6	Thermocouples 1 and 2	28
3-7	Thermocouples 4 and 5	29
3-8	Thermocouples 6 and 7	29
3-9	Thermocouples 4 and 6	30
3-10	Anti-buckling guide	31
3-11	Strain gauge placement	32
3-12	Anti-buckling guide verification results	33
3-13	Extensometer set-up	34
3-14	Extensometer and anti-buckling guide assembly (plan view)	35
3-15	Extensometer and anti-buckling guide assembly (side view)	36
3-16	Close up of extensometer.	37
3-17	Extensometer verification results on a steel specimen	38
3-18	Specimen lay out	40
3-19	Cyclic waveforms	41
3-20	Load profile for TiGr test	42
3-21	Comparison between stiffness measurements for two load ranges	43

3-22 Specimen section diagram	44
4-1 Load vs. strain for OHT test 3	48
4-2 OHT test specimen after failure	49
4-3 Facesheet crack pattern	50
4-4 Cross-section schematic for micrographs	50
4-5 Micrograph of titanium delamination in the outer ply	51
4-6 Micrograph of titanium delamination in the outer ply	51
4-7 Micrograph of 0° ply splitting	52
4-8 Micrograph of 90° ply cracks	53
4-9 Stiffness loss for damage progression specimens	54
4-10 Sketch of damage after 1,000 cycles	56
4-11 Sketch of damage after 10,000 cycles	56
4-12 Sketch of damage after 30,000 cycles	57
4-13 Sketch of damage after 100,000 cycles	57
4-14 Sketch of damage in delaminated specimen	59
4-15 Front view of specimen that failed via fracture	60
4-16 Schematic of fracture failure	60
4-17 Side view of specimen that failed via fracture	61
4-18 Damage region near hole after failure via fracture	61
4-19 Fatigue life data for TiGr 2-6-2	63
4-20 Stiffness vs. cycles at seven stress levels	64
4-21 Residual strength vs. stiffness loss	65
4-22 Stiffness loss vs. cycles at room temperature (30% OHT, R=-0.2) and 350° F	66
5-1 Stress concentration in notched TiGr 2-6-2	69
5-2 Stress concentration for an isotropic sample	70
5-3 S-N data for titanium 15-3-3-3, $K_t = 3$, 400° F	71
5-4 First crack data for TiGr 2-6-2	73
5-5 Schematic of delamination growth	75

5-6	X-Ray of damage in 24 mm wide, AS4/PEEK cross-ply laminate	76
5-7	Split length vs. cycles in AS4/PEEK cross-ply laminate	77
5-8	Schematic of strain energy release rate calculation	79
5-9	Normalized strain energy release rate for four facesheet materials	81
5-10	Crack growth vs. ΔG for APC2	82
5-11	Schematic of stiffness model	83
5-12	Effect of damage on measured stiffness	85
5-13	Damage growth rate as a function of stress level	87
5-14	SERR for alternative lay-ups	90

List of Tables

- 3.1 Material properties 24
- 3.2 Polishing sequence (approximate) 45
- 4.1 Open hole tension test results 47
- 5.1 Material properties for strain energy release rate comparison 80
- 5.2 Stress concentration for alternate laminates 89

Chapter 1

Introduction

The High Speed Civil Transport (HSCT) is projected to fly at Mach 2.4. At this speed, skin temperatures can reach 350° F, which precludes the use of aluminum as the primary structural material due to its inadequate creep resistance. In addition to being able to withstand high temperatures, the skin material also must operate in a harsh environment, resisting oxidation at cruise altitude and moisture ingress on the ground, while maintaining structural integrity for a service life of 60,000 hours. To satisfy the requirements for an HSCT skin material, The Boeing Company is developing titanium-graphite hybrid laminates (TiGr).

1.1 Hybrid Laminates

Hybrid laminates such as TiGr, sometimes called fiber metal laminates (FML), are made up of polymer matrix composite (PMC) plies interspersed with metal foil. The two materials are combined by bonding the PMC plies and metal foils to form a composite laminate. In this project, the TiGr laminate consisted of a PMC core with titanium foils as the outer plies. A schematic of this TiGr laminate is shown in Figure 1-1.

Hybrid laminates combine the attractive aspects of the two constituent materials and avoid some of the weaknesses. Use of titanium as the outer plies protects the

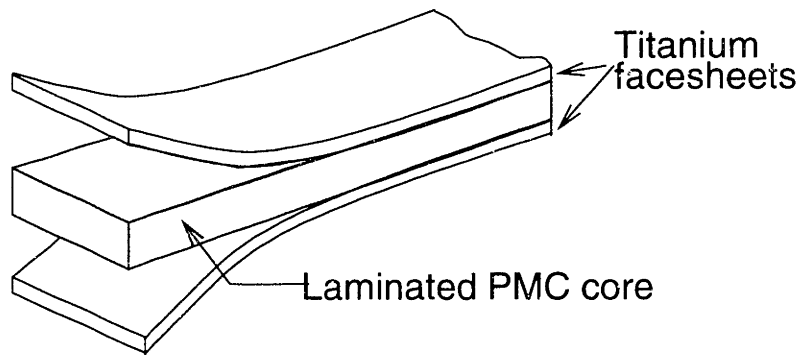


Figure 1-1: TiGr laminate

PMC core from environmental effects such as oxidation and moisture ingress. The composite core has higher strength and stiffness to weight ratios than titanium and is presumed to be less sensitive to fatigue effects. The combination of the two materials as a hybrid composite could potentially outperform either of the two constituent materials in HSCT applications and other elevated temperature structural applications.

1.2 Objectives

Hybrid laminates are a relatively new material technology, therefore, the material behavior needs to be characterized before such materials can be used in practical applications. The ultimate goals of the TiGr research program are to develop a material property database, guide material development, and develop a design methodology that can be used in applying hybrid laminates to structural applications.

The particular objective of the work documented in this thesis was to conduct elevated temperature (350° F), cyclic loading tests on TiGr laminates, record fatigue life data, and observe the key failure mechanisms. Open hole specimens were chosen as being representative of severe impact damage or mechanical fasteners, which are likely sites for damage initiation in fatigue loading conditions. By studying the progression of damage and recording the stiffness loss during fatigue cycling, insights were obtained into the relative importance of the different damage modes and how

they interact. First order comparisons were made between the fatigue damage mechanisms of TiGr laminates and the fatigue damage mechanisms of the constituent materials and the interactions between them. While the ultimate goal of the overall research program on hybrid composites is to develop material and structural design philosophies, the immediate impact of this project will be to guide the design of longer duration test programs and to identify potentially fruitful directions for material development.

Chapter 2

Background

2.1 Overview of Hybrid Laminates

Hybrid laminates were developed in the early 1980's at Delft University in The Netherlands. Originally the Delft research group developed ARamid Aluminum Laminates (ARALL) as a fatigue resistant material. ARALL is produced commercially by the ALCOA company. The successor to ARALL was Glass Fiber Aluminum Laminates (GLARE), also developed at Delft University. TiGr was developed by engineers at The Boeing Company in the early 1990's with the goal of developing a material with the same favorable fatigue properties as ARALL and GLARE, but useful for higher temperature applications.

2.1.1 ARALL and GLARE

ARALL was first developed to be a fatigue insensitive material for use in tension-dominated, fatigue critical structures on aircraft. Benefits include 15-20% lower density than aluminum and up to 60% higher strength than comparable aluminum (2024 or 7075 series) structures [1]. Commercially, ARALL is available in four types. Each type uses a different aluminum alloy and has properties tailored for specific uses, e.g. ARALL-1 uses 7075-T6 as the aluminum alloy and is best suited for high fatigue loaded structures with large compressive regimes while ARALL-2 uses 2024-

T3 aluminum and is geared toward applications requiring high damage tolerance and formability. ARALL laminates are nominally given a 0.4% permanent stretch to nullify the residual stresses that arise from the curing process [1].

ARALL has been studied for a number of aerospace applications. Successful tests were performed on a prototype wing panel for the Fokker F-27. Studies showed that using ARALL on the outboard lower wing structure for the Fokker F-27 produced a possible 30% weight savings [2]. Fokker also used ARALL laminates on the F-50 prototype aircraft [1]. ARALL was also used in the redesign of a cargo door for the C-17 military transport, producing a 23% weight savings [3].

Since ARALL was designed as a “fatigue resistant” material, a significant amount of research has been performed on the fatigue properties. Much of the research has been focused on the effects of fiber bridging of cracks in hybrid laminates. Fiber bridging occurs when a crack forms in the laminate, but intact fibers remain behind the crack, effectively reducing the stress intensity factor at the crack tip. This behavior is one reason for the superior fatigue resistance of hybrid laminates.

A number of researchers have experimentally studied the effect of crack bridging in hybrid laminates. Ritchie et al. conducted studies of crack growth rate and the fiber bridging effects [4]. They found that crack growth rates in the aluminum plies of ARALL-2 are up to three orders of magnitude lower than those in monolithic aluminum at the same applied stress intensity factor. They also found that a bridging zone, between three and five millimeters long, exists in the wake of the crack tip which was promoted by controlled delamination at the fiber/epoxy interface. They determined that the crack growth rates were not dependent on the applied stress intensity factor amplitude, ΔK , due to the crack bridging effects. They derived an experimental and analytical procedure to determine an effective stress intensity factor amplitude, ΔK_{eff} , that incorporates fiber bridging and crack closure effects and can be used to predict crack growth rates at arbitrary stress levels.

Toi and Fujiwara, [5] developed a “slow crack growth model” to classify the crack growth behavior in GLARE laminates. They claim the method is simpler for designers to use because it is based on a Paris type equation for crack growth and uses an

empirically determined “knock down factor” on the applied stress intensity factor. This eliminates the need for complex analysis of fiber bridging.

Salivar and Gardini [6] investigated the effect of temperature on crack growth rates in ARALL-3. In the panels tested at room temperature the crack growth rate initially decelerated and then accelerated as the stress intensity factor amplitude, ΔK increased. At elevated temperatures, the crack growth rate only decelerated as ΔK increased. They attributed the difference to the different fiber behavior at room temperature vs. elevated temperature. Residual strength tests were performed on the fatigued specimens and for the high temperature tests, there was very little residual strength loss due to fatigue.

Osiroff et al. [7] investigated the fatigue of ARALL and identified the damage sequence for the laminates during fatigue loading and studied the effects on stiffness and strength.

Many researchers (Papakyriacou et al. [8], Roebroeks [9], Bertheau et al. [10]) have performed similar research on the fatigue response of ARALL and GLARE, and have essentially reached the conclusion that ARALL and GLARE possess superior fatigue properties over monolithic aluminum. The crack growth rates in the material decrease, and in some cases complete crack arrest occurs, as a result of the intact composite fibers bridging the cracks in the aluminum plies and reducing the effective stress intensity factor at the crack tips.

Lee and Wilson [11] studied the impact behavior of ARALL-2 at different temperatures and found that there was a significant effect of temperature on the material response. The experiment at 75° F had the lowest internal damage area, but absorbed the highest impact energy and exhibited the lowest residual strength. The specimen tested at the highest temperature, 280° had the highest residual strength. The authors hypothesized that as temperature increased, the number of fibers damaged due to impact decreased and since the residual strength is mainly governed by fiber strength, the residual strength was higher.

Sun et al.[12] developed a method for predicting the residual strength after impact in ARALL laminates based solely on the depth of the impact damage. This allows a

prediction of residual strength after impact based on a visual inspection of the damage region.

Finite element models have been developed for hybrid laminates. Hashagen et al. [13] developed a geometrically and physically nonlinear solid-like shell element to analyze the behavior of hybrid laminates. Marissen [14] developed an analytical finite element approach to predict crack growth behavior. The model incorporates many of the material variables in ARALL and the author claims that it could be used in the development of similar materials.

Pettit [15] developed a damage tolerance philosophy for use with hybrid laminates. He classified cracks in the exterior facesheets as “nuisance cracks” because they have little effect on the overall strength and stiffness of the material. He proposed using a fatigue criterion in which the structure is assumed to be capable of sustaining limit loads for four lifetimes of load cycles and a residual strength criterion in which the structure is assumed to be capable of sustaining ultimate loads for one lifetime. He also incorporated a maximum length for “nuisance cracks” over the lifetime of the structure, to account for the sensitivity amongst airlines and passengers to the appearance of the structure.

2.1.2 TiGr

Since TiGr laminates are relatively new, the database of previous research is limited. Most of the work has been conducted by The Boeing Company and consequently is unavailable to the public due to restrictions on the release of company proprietary information.

One of the major concerns regarding TiGr laminates is the durability of the bond between the PMC core and the titanium facesheets. In 1994, a study was conducted by Miller, et al. on the mechanical response of hybrid titanium composite laminates [16]. They determined that the bond quality between the plies affects both the static and fatigue properties. A poor bond can reduce the ultimate tensile strength, but can improve the fatigue behavior. They determined that hybrid laminates perform much

better in fatigue than monolithic titanium. In similar fatigue tests performed by Li and Johnson in 1996 fatigue cycling caused adhesive failure between the titanium plies and the PMC core, indicating a weak bond [17].

As for ARALL and GLARE, a major research focus has been fatigue cracking of the facesheets. Due to the role of the facesheet in providing environmental protection of the PMC core, this is a major concern in TiGr laminates. Miller et al., mentioned the facesheet cracks but did not discuss them in detail since they did not cause ultimate failure. In studies by Li and Johnson, the fatigue behavior of the facesheets was compared to that of monolithic titanium. They found that although Ti-15-3 has better monolithic fatigue properties than Timetal-21s, when placed into hybrid laminates, their performance is similar. In the fatigue tests of the laminate, multiple cracks formed in the titanium layers due to the bridging behavior of the fibers. When a crack formed, load was transferred to the underlying fibers via interlaminar stresses. The intact PMC layers continued to carry load, so multiple cracks formed in the titanium layers.

Parametric analytical studies were conducted by Johnson, et al. to study the effects of varying the laminate stacking sequence, fiber volume fraction, the choice of fiber type, and the percentage of titanium in the lay-up [18]. They concluded that one of the key points in designing a hybrid laminate is to ensure the PMC core has a higher modulus than the facesheets in order to take advantage of the superior strength and stiffness properties of the PMC. Otherwise, the drawbacks in using a complex material system such as a hybrid laminate may outweigh the benefits. They commented that parametric studies are useful, but more testing is needed.

2.2 Fatigue of Metals

Metal fatigue was first identified in the mid-19th century when railcar axles failed under repeated stresses and has been an active research field ever since. Wöhler studied failure under repeated loads and developed the concept of the stress-life or S-N curve as a design tool [19]. Wöhler used S-N curves to define a fatigue limit, a

stress level below which the material will not fracture. S-N curves are based entirely on empirical data and the fatigue limit is the stress level at which the material is not expected to fail after a large number of cycles, usually on the order of 10^6 or 10^7 [20].

A related design methodology using S-N curves is the total-life or safe-life approach. In this approach, S-N data is used to define the fatigue life at specific stress or strain levels. After reaching the design life, the part is retired from service. This approach is commonly used in the design of helicopter and turbine blades. Since many applications have a varied loading spectrum, a single S-N curve can not be used for design purposes. Once a load spectrum is developed for a certain part, Miner's Rule is a common method used to design for safe-life.

Using airplane design as an example, the loading spectrum defines how many cycles of each load type are expected to be applied to a component during each flight. Miner's Rule is shown in Equation 2.1 where D is the damage state, N_{blocks} is the number of flights in a given component's lifetime, n_i is the number of cycles at the i th load level, and N_i is the total life in the i th load level as found from S-N data [20].

$$D = N_{blocks} * \sum \frac{n_i}{N_i} \quad (2.1)$$

A component has no damage when D equals 0 and is considered failed when D equals 1. Miner's rule assumes that damage is an additive quantity and that loading sequence has no affect on life. The scatter generally associated with S-N data requires that a large factor of safety, usually on the order of four, be applied when using Miner's Rule.

With advances made in fracture mechanics over the past fifty years, new methods for fatigue design have been developed. Damage tolerant design for fatigue assumes that flaws exist in the material. Components are designed such that the smallest flaw visible using non-destructive testing techniques will not grow to catastrophic lengths between inspection intervals. Normally, a factor of safety of two is used such that the flaw can not grow to failure during two inspection intervals. One of the method's used to predict crack growth is Paris' Law (Equation 2.2), which is based on the cyclic

amplitude of the stress intensity factor, K and two empirically determined constants, A and n [19].

$$\frac{da}{dN} = A(K)^n \quad (2.2)$$

The life of a component can be predicted by integrating the Paris equation from the initial flaw size to the final flaw size. In theory, a component designed using a damage tolerant approach can have an infinite fatigue life so long as regular inspections are conducted that do not detect fatigue crack growth. Other variants on Paris' Law, such as the Forman equation [19], incorporate mean stress into calculations for fatigue crack growth.

2.3 Fatigue Effects in Polymer Matrix Composites

The fatigue behavior of polymer matrix composites (PMC) is more complex than the fatigue of metals due to the occurrence of multiple, interacting damage modes. A significant amount of research has been conducted to characterize and model the effect of fatigue on composite materials. This section provides a brief summary of the major characteristics of fatigue in composites.

Many damage modes such as transverse ply cracks, fiber-matrix debonding, matrix crazing, and microbuckling occur as a result of cyclic loading on composite materials [21]. However, ply splitting and delamination are the two major factors that influence strength and stiffness in notched PMC materials. In general, these damage modes arise because of the inhomogeneous nature of composite laminates. Since the fibers are generally not susceptible to fatigue failure, the matrix material is the dominant element for fatigue damage.

In notched composites, fatigue damage initially appears as ply splits that run in the 0° plies, tangential to the hole, and parallel to the loading axis [21]. This type of damage was observed by Spearing, et al. [22] in cross ply laminates. They used a Paris type relation to characterize the growth rate of the splits as a function of the

strain energy release rate [23]. The researchers determined that thicker ply groups increase the split growth rate. It was also shown that the residual strength of a laminate increases as a result of the ply splits and associated damage, because the damage region acts to blunt out the stress concentration due to the notch [24].

Delamination between the ply groups is the second major damage mode in notched laminates. Delamination can form at free edges or as a result of other damage types or as a result of the interlaminar stresses [25]. Several researchers have shown that delamination growth in fatigue can be described by a Paris type relationship [26]. The presence of delamination can significantly reduce the overall stiffness of the laminate. Spearing et al. developed a model for delamination growth under cyclic loads in conjunction with ply splitting [23]. Dahlen and Springer developed a semi-empirical model to describe general delamination growth in composites [27].

2.4 Summary

Fatigue behavior of both metals and polymer matrix composites is still a very active research field. Fatigue behavior of TiGr laminates combines aspects of both materials. Cracks form and propagate in the metal facesheet layers, but the crack behavior is linked to the properties of the PMC core. The splitting and delamination that form in the PMC affect the behavior of the facesheet. Additional research needs to be done on TiGr laminates to characterize the interactions between the two constituent materials. The models that were developed for ARALL and GLARE should be applied to TiGr laminates to determine if they provide a valid description of the behavior. In addition, more research needs to be performed to fill in the gaps in TiGr research database. Very few tests have been conducted on the high temperature behavior of TiGr and the damage progression in TiGr laminates.

Chapter 3

Experimental Procedure

To determine the S-N behavior of Ti/Gr laminates, a mechanical test program was conducted at The Technology Laboratory for Advanced Composites (TELAC) in the Department of Aeronautics and Astronautics at the Massachusetts Institute of Technology. This chapter provides a description of the specimens and the verification of the equipment and procedures used in the test program.

3.1 Test Specimens

The specimens were 12" x 1.5" rectangular coupons with a 0.25" diameter hole in the center. The facesheets were made from 0.005" thick Titanium 15V-3Cr-3Al-3Sn (Ti 15-3) foil and the polymer matrix composite (PMC) core consisted of an IM-7/PIXA cross-ply laminate with a ply thickness of 0.0054" and a fiber volume fraction of approximately 0.6. Ti 15-3 is a metastable beta titanium alloy chosen for its low density and minimum processing and fabrication costs [28]. IM-7 is an intermediate modulus graphite fiber. PIXA is thermoplastic polyimide resin [29] with a very low fraction of volatile species. In most composite materials, volatiles can escape during the cure cycle, however in TiGr laminates the titanium facesheets prevent this. If the vapor pressure of volatiles was too high, voids would result in the material.

In all the specimens tested, the lay-up was $[\text{Ti}/0/90/0_2]_s$, a high strength configura-

tion intended for use in fuselage crown panels. A schematic of the specimen is shown in Figure 3-1. The specimens tested in this project were taken from two batches of material. The only nominal difference between the two batches of specimens was a decrease in length of 1" for the second set of specimens. Material properties for the constituent materials and for the laminate are given in Table 3.1. The constituent properties were supplied by The Boeing Company [30] and the laminate properties were calculated using Classical Laminated Plate Theory (CLPT).

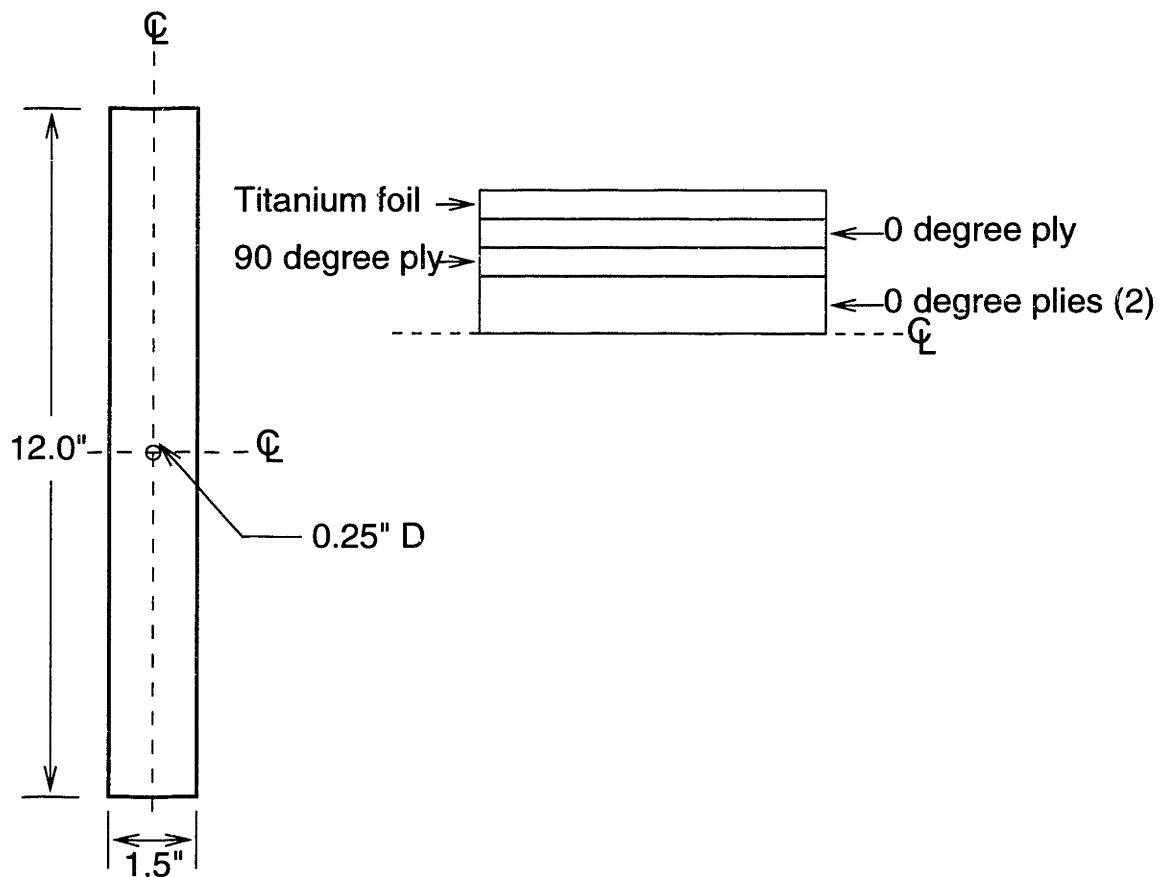


Figure 3-1: Test specimens

The specimens were manufactured by The Boeing Company in Seattle, WA using a company proprietary procedure. Boeing manufactured the specimens out of four panels 24" wide and 14" long. An abrasive waterjet was used to cut the coupons to the final size. Out of the 54 total specimens, 44 had the 0.25" hole in the center and 10

Table 3.1: Material properties

Material Property	Ti 15-3	IM-7/PIXA	TiGr 2-6-2
E_1 (Msi)	15.5	23.5	17.7
E_2 (Msi)	16.3	1.0	8.8
G_{12} (Msi)	6.0	0.65	1.66
ν_{12}	0.33	0.35	0.162

were unnotched.

3.2 Test Equipment

3.2.1 Load frame

The tests were carried out on an Instron 1332 servohydraulic load frame with a maximum capacity of 50,000 lbs. The load frame was controlled using an 8500+ digital controller. The load frame was equipped with water cooled grips to allow high temperature testing. A photograph of the load frame and controller is shown in Figure 3-2.

3.2.2 Temperature cabinet

The temperature cabinet was based on a design by Fisher et al. [31]. The cabinet is constructed out of aluminum sheet and insulated with structural board insulation. A schematic of the cabinet is shown in Figure 3-3. It is heated using a Royal 1000W heat gun. The temperature in the cabinet is controlled using an Omega 5002K temperature controller. One thermocouple, offset by approximately 1.5" above the hole, was used to control the temperature. At the test temperature of 350° F the cabinet is controlled to +/- 1° F. A photograph of the cabinet set-up installed on the load frame is shown in Figure 3-4.

In order to verify the performance of the cabinet and the controller, a verification

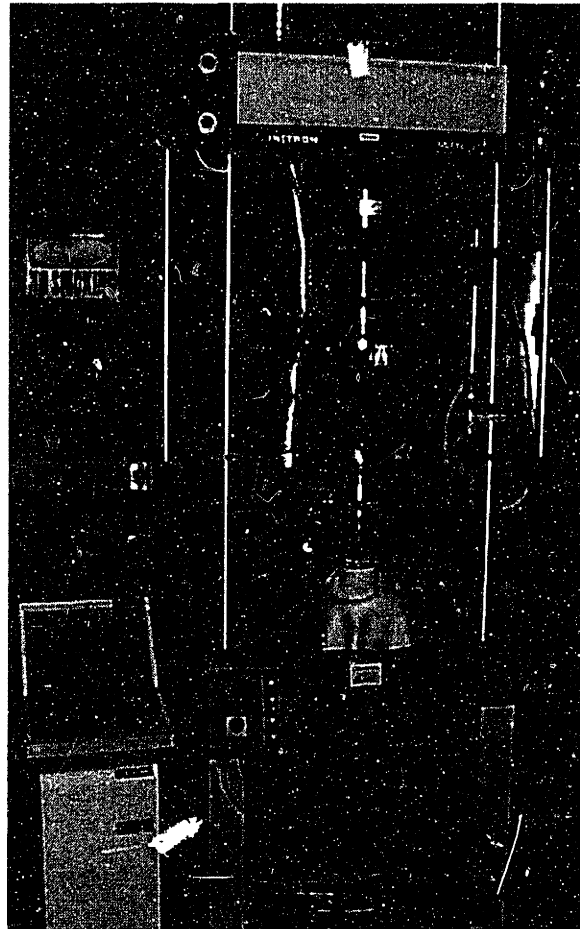


Figure 3-2: Load frame and controller

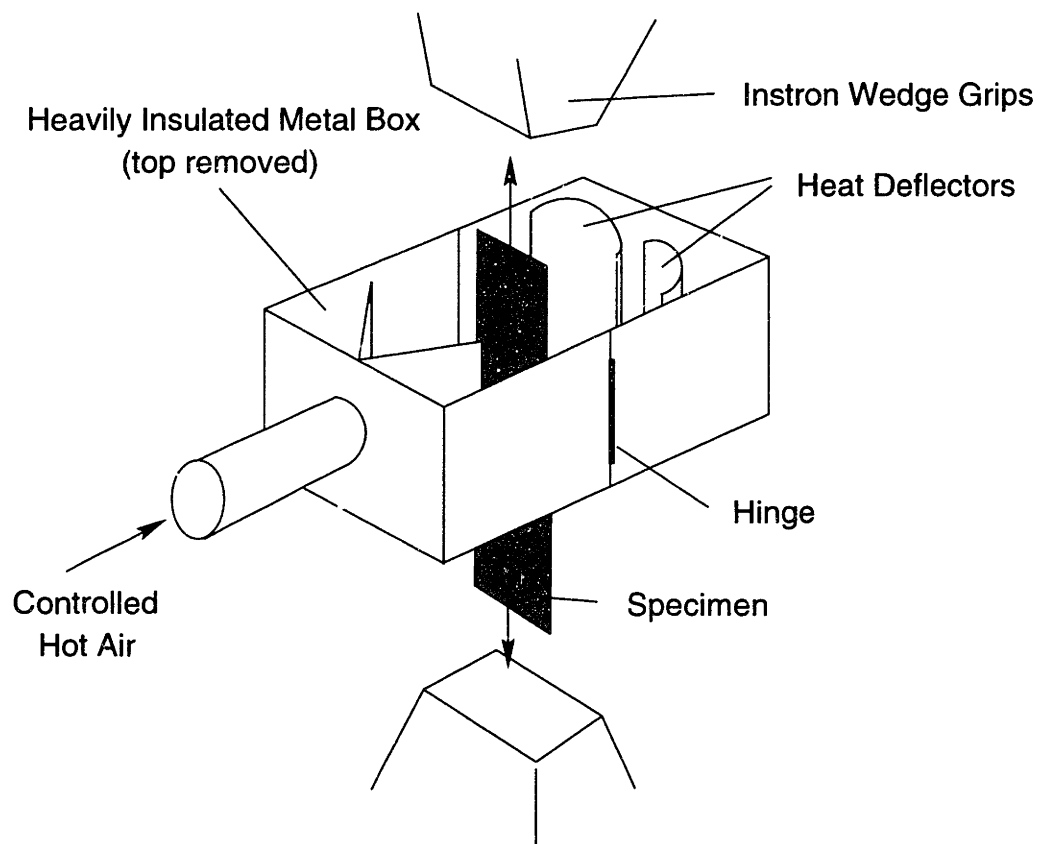


Figure 3-3: Temperature cabinet

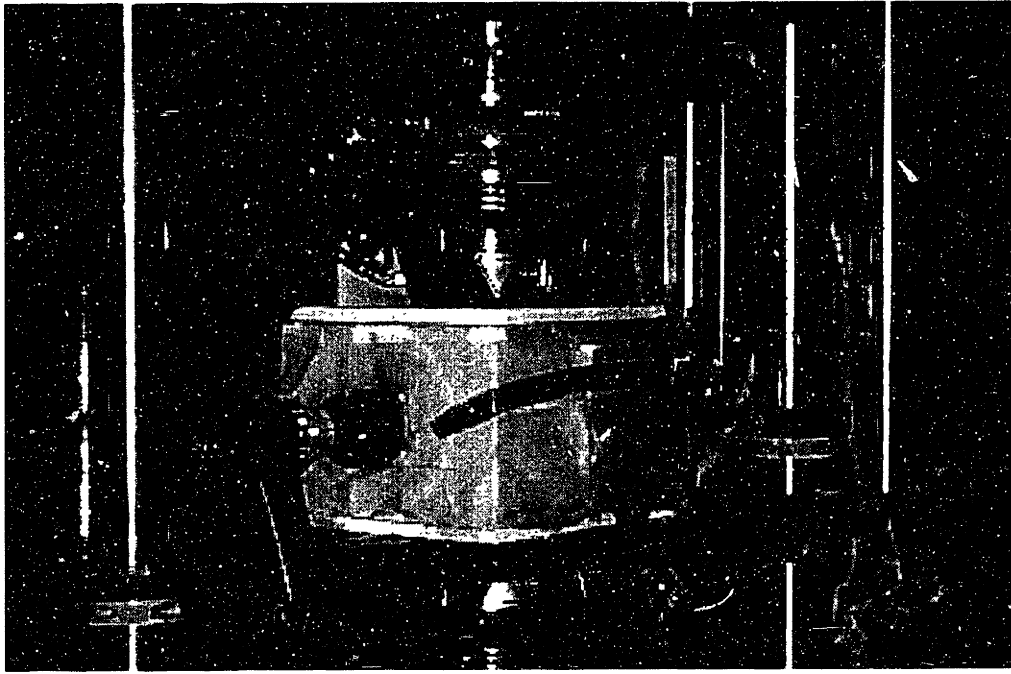


Figure 3-4: Cabinet set-up

test was run on the test setup. Thermocouples were mounted on a TiGr specimen as shown in Figure 3-5. The assembly was then placed in the temperature cabinet and heated. The thermocouples were connected to a Power Macintosh computer via an A/D board and the temperature versus time data was recorded using the LabVIEW software package.

The test showed that the temperature differential between the top and bottom of the cabinet was less than 5° F and there was a variation of less than 1° F from front to back. Figures 3-6, 3-7, and 3-8 show the comparison between front and back thermocouple pairs and Figure 3-9 shows the comparison between a thermocouple near the center and one near the bottom edge.

3.2.3 Anti-buckling guide

An anti-buckling guide was necessary to prevent instabilities during compression testing. The design for the stainless steel anti-buckling guide was provided by Boeing

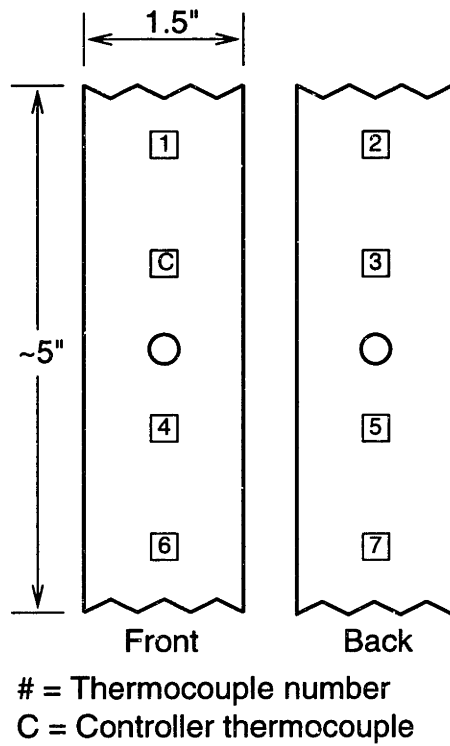


Figure 3-5: Thermocouple placement

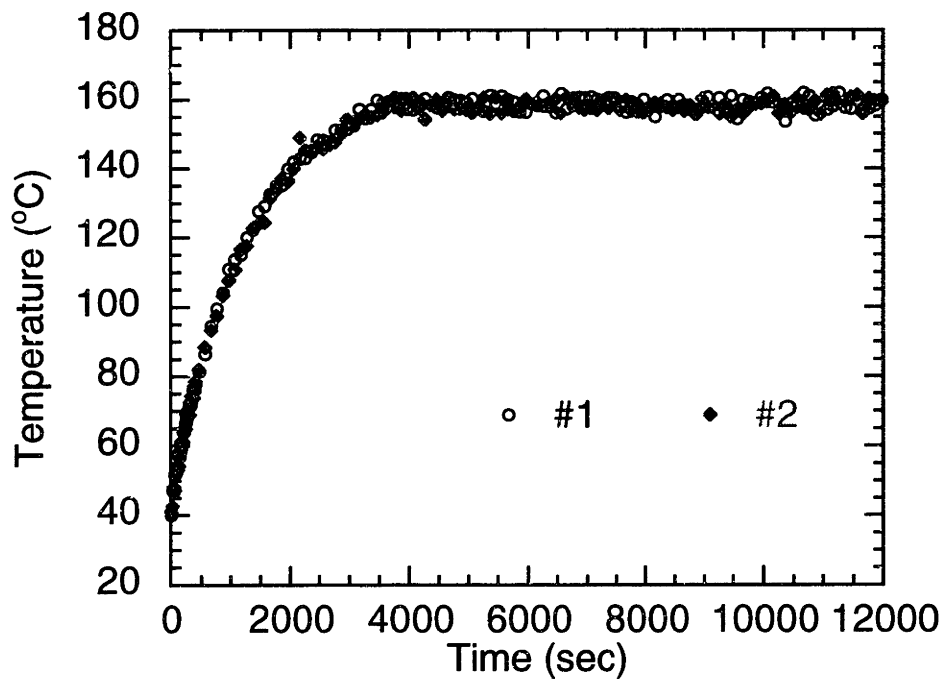


Figure 3-6: Thermocouples 1 and 2

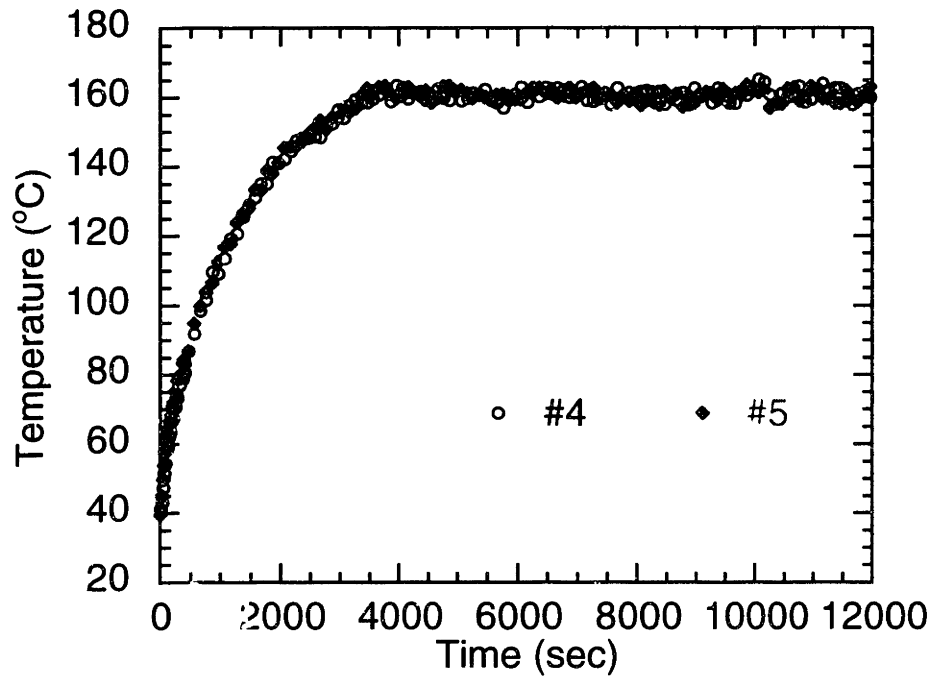


Figure 3-7: Thermocouples 4 and 5

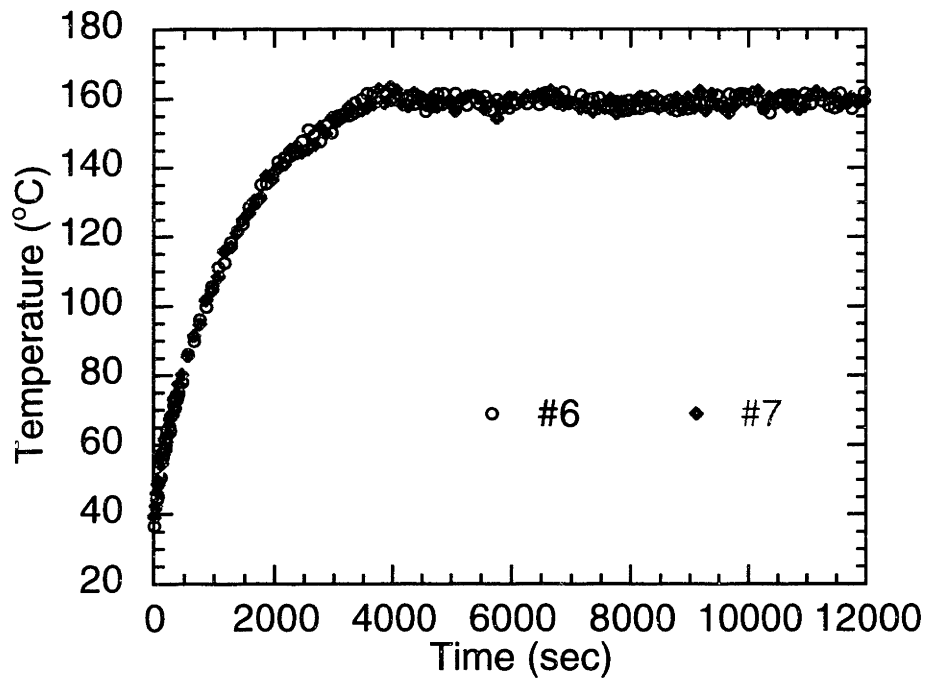


Figure 3-8: Thermocouples 6 and 7

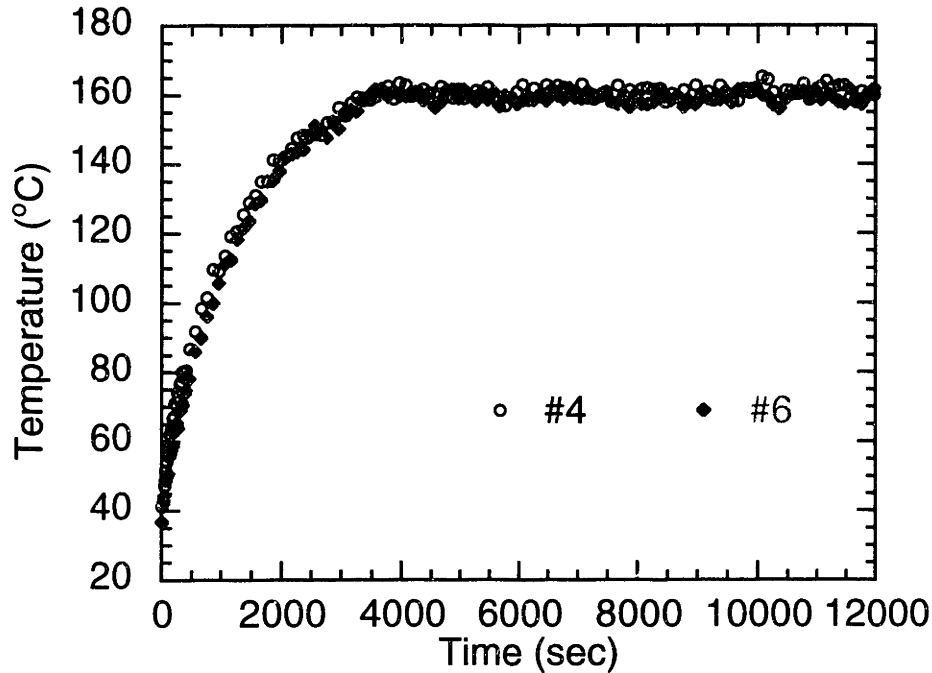


Figure 3-9: Thermocouples 4 and 6

and a schematic of the design is shown in Figure 3-10. The groove for the specimen was sized for the specific lay-up used in the test program in order to minimize the interference between the specimen and the anti-buckling guide.

To confirm that the anti-buckling guide provided the necessary support to prevent instabilities and did not interfere with the loading cycle, a series of tests were performed. The first test involved attaching strain gauges to the front and back of the specimen to verify that the anti-buckling guide provided the necessary support. A schematic of the strain gauge placement is shown in Figure 3-11. The specimen was placed in the load frame with the anti-buckling guide installed and then quasi-statically loaded in compression to 3000 lbs, which is higher than the maximum compressive load applied during fatigue tests. If the anti-buckling guide did not prevent the specimen from buckling or if the load frame grips were not properly aligned, this would result in a divergence in the measured strain between the front gauge and the back gauge. In addition, if the anti-buckling guide did not allow free movement of the specimen, it would show up as discontinuities in the data, or hysteresis between

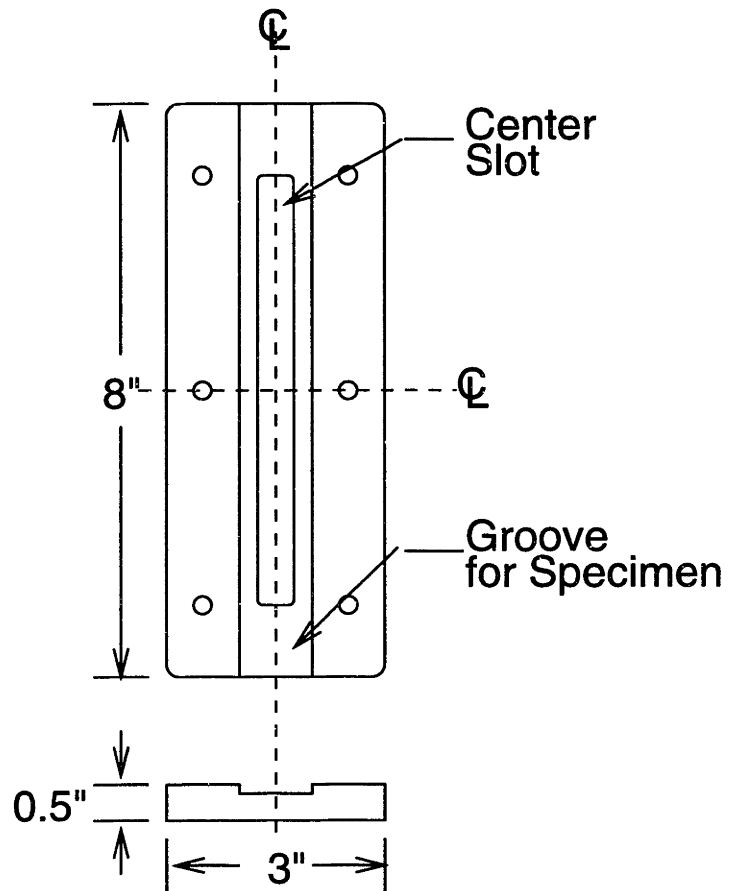


Figure 3-10: Anti-buckling guide

loading and unloading.

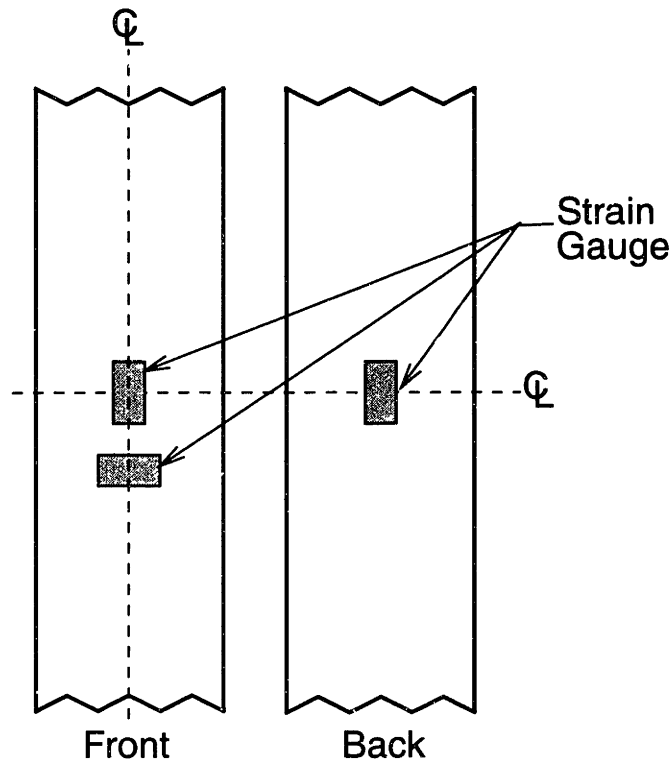


Figure 3-11: Strain gauge placement

A bending strain parameter was defined as the difference between the strain measured with the front gauge and the strain measured with the back gauge normalized by the sum of the two measured strains $(\text{front} - \text{back})/(\text{front} + \text{back})$. This parameter is plotted versus load in Figure 3-12 for one of the test runs. The plot shows the bending strain varying by less than 5% over most of the load range. The high peaks at the lower load levels were due to noise in the system at small loads. Initially, a small amount of sticking occurred between the specimen and the anti-buckling guide. The problem was alleviated by coating the groove in the anti-buckling guide with a thin layer of high-temperature silicon-based grease in early tests and a layer of spray-on graphite lubricant in later tests.

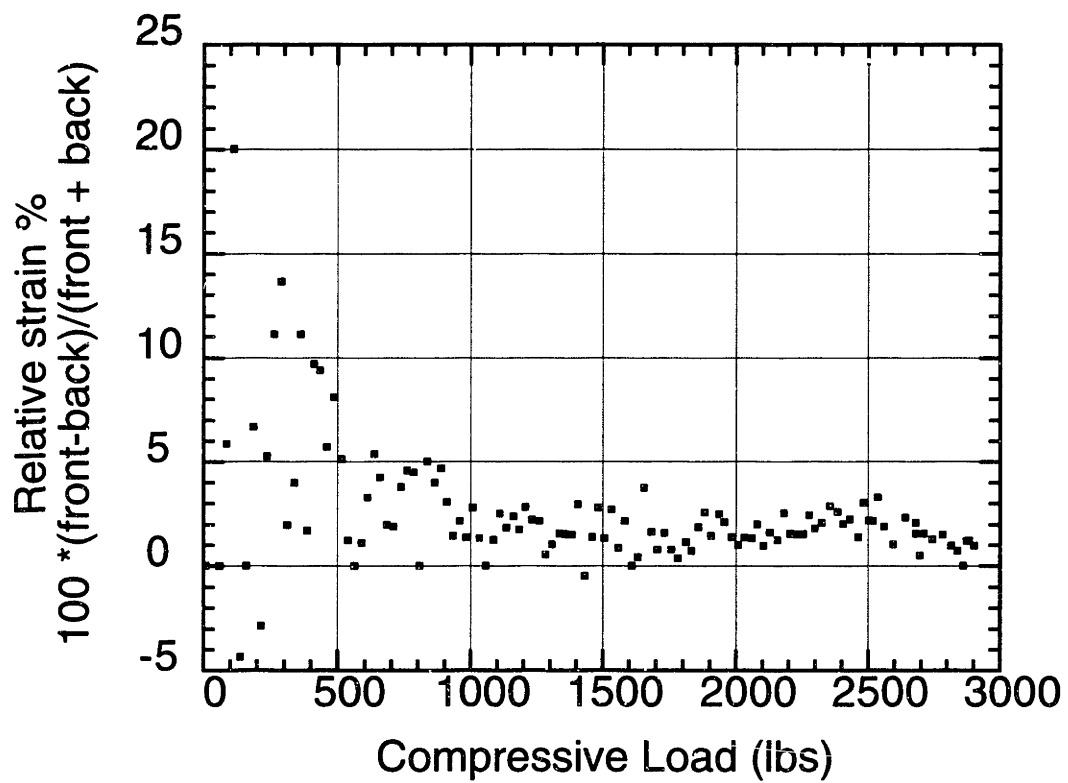


Figure 3-12: Anti-buckling guide verification results

3.2.4 Extensometer

To monitor the stiffness loss of the specimens during the cycling, a high temperature extensometer (Instron model # 2620-827) was used. The extensometer was held in place using a spring loaded plate attached to the anti-buckling guide as shown in Figure 3-13. A picture of the extensometer and anti-buckling guide assembly is shown in Figure 3-14 and Figure 3-15. A small bead of Epoxi-Patch was applied to the specimen on either side of the knife edges to prevent slippage during cyclic loading as shown in Figure 3-16.

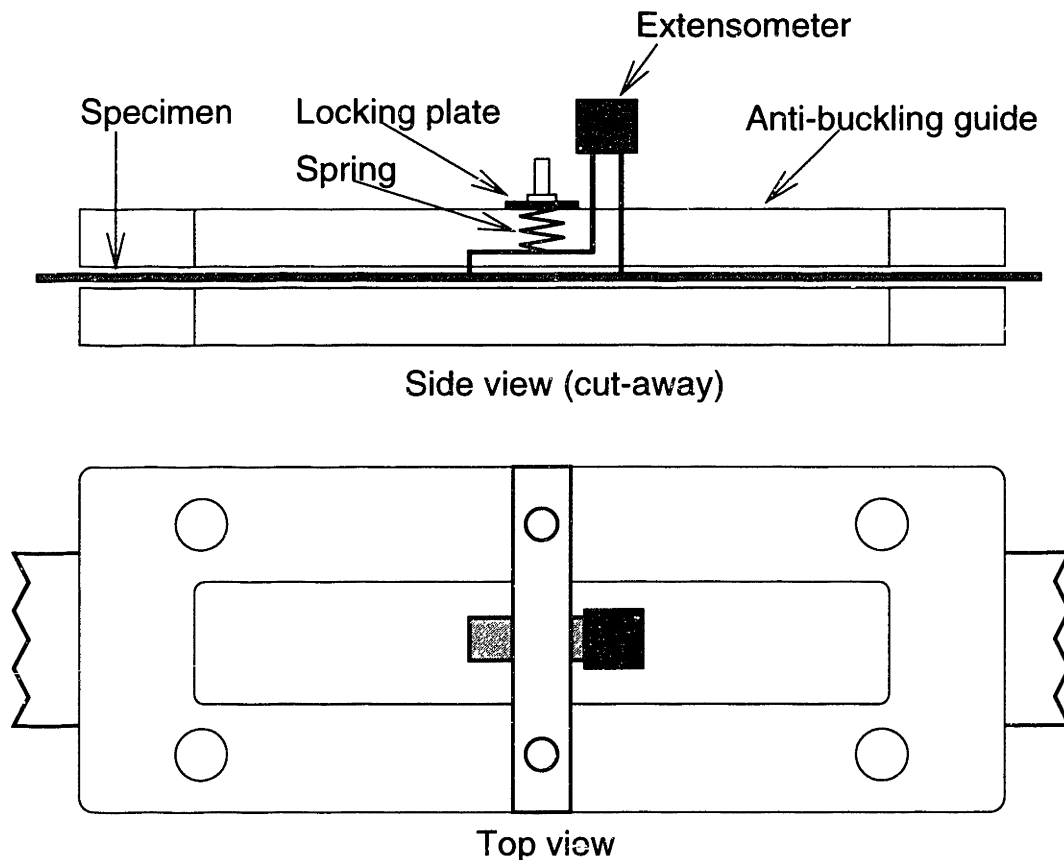


Figure 3-13: Extensometer set-up

Verification of the effectiveness of the anti-buckling guide was achieved using a steel plate sized to approximately the same dimensions as the TiGr specimens. The

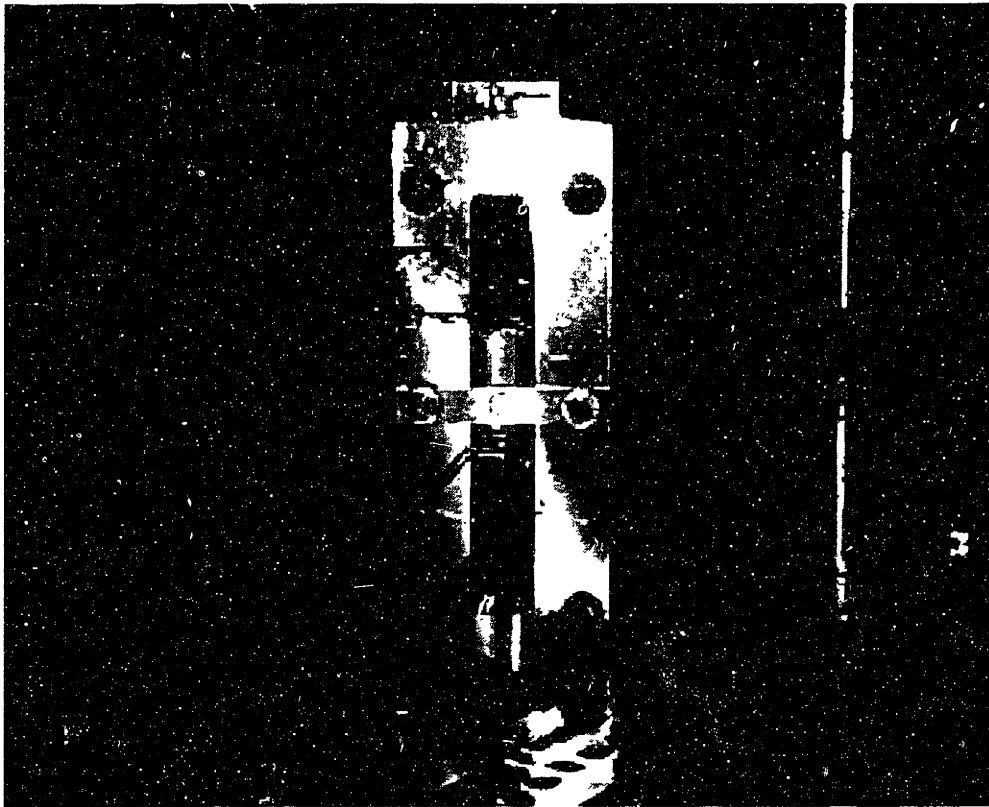


Figure 3-14: Extensometer and anti-buckling guide assembly (plan view)

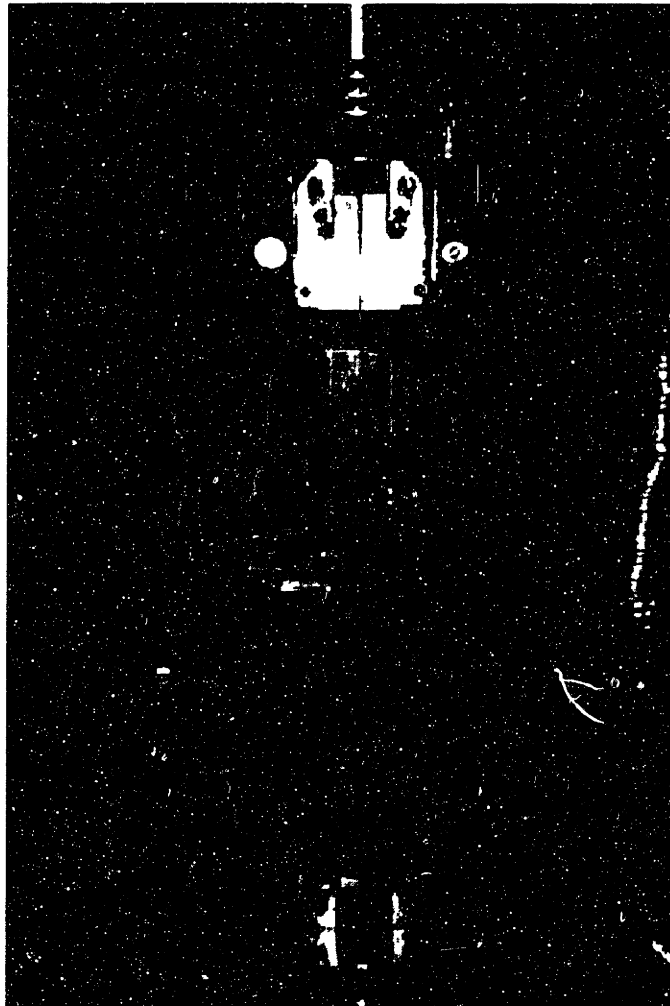


Figure 3-15: Extensometer and anti-buckling guide assembly (side view)

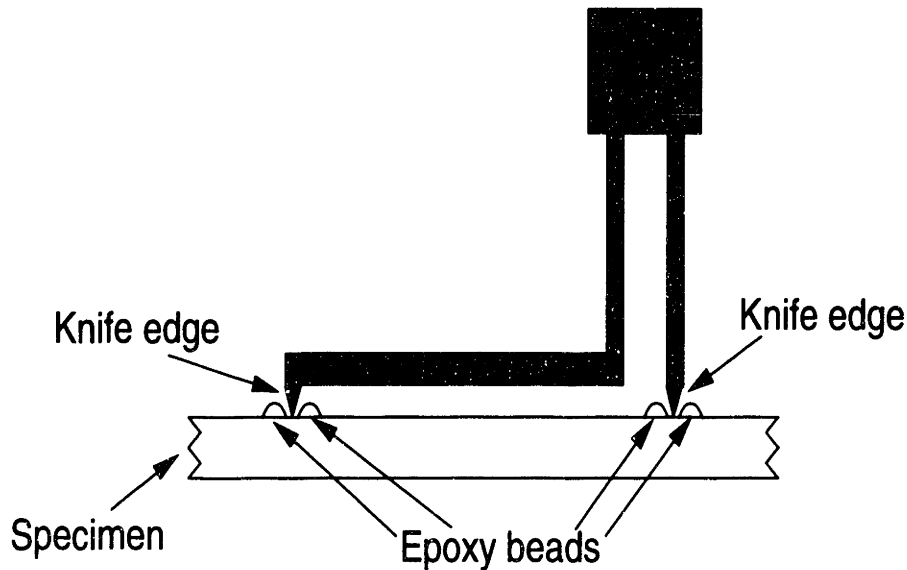


Figure 3-16: Close up of extensometer.

plate was cycled in fatigue at load levels similar to the TiGr testing and then slowly ramped to the maximum load to measure stiffness. The premise behind the test is that steel should not incur fatigue damage at the test loads. Figure 3-17 shows the data for the steel plate test. Two sets of data are shown, one in which the stiffness was normalized by the stiffness measured in the first cycle and one where the stiffness was normalized by the stiffness after 1,000 cycles. In the first set, a large jump in the relative stiffness occurs. It is believed that this is because the extensometer was not settled properly in the epoxy grooves. This hypothesis is substantiated by two observations, firstly that after the initial jump, the stiffness is constant and secondly that, when normalized by the stiffness after 1,000 cycles the relative stiffness is within the expected range. The subsequent deviation in the data is much smaller than the stiffness losses expected during TiGr testing.

3.3 Test Procedure

The majority of the tests conducted were high-temperature, tension-compression fatigue tests. General procedures were developed for this type of test and modified as

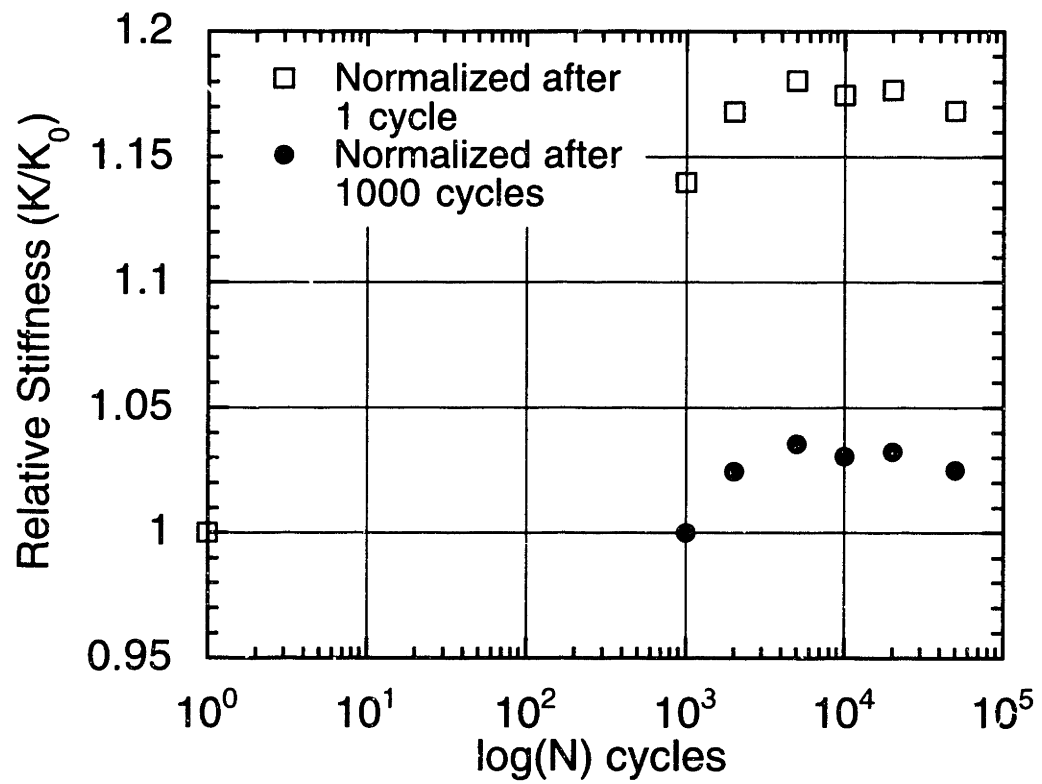


Figure 3-17: Extensometer verification results on a steel specimen

noted below for the other type of tests that were conducted.

3.3.1 Specimen preparation

Before testing, the specimens were cleaned and prepared. The surface of the titanium was wiped with isopropyl alcohol to remove any grease and dirt. Inserts of emery cloth were attached around the specimen ends with flash tape to prevent the serrated grip faces from damaging the titanium foil. The inserts were just under 1.5" wide, to prevent them from interfering with specimen alignment, and 3" long, extending 1.5" on each side of the specimen when folded around the end. The emery cloth inserts were also used as a guide for centering the specimen between the grips. A K-type thermocouple lead was attached to the specimen surface just above the hole. The thermocouple was used to monitor the temperature in the temperature cabinet and provide the temperature input for the heat gun controller. Figure 3-18 shows the resulting specimen configuration.

3.3.2 Fatigue test procedure

After attaching the thermocouple and the emery cloth inserts, the specimen was inserted into the load frame. The grips were approximately 9" apart and the top grip was clamped first. For the fatigue tests an approximate grip pressure of 3000 psi was applied. Once the specimen was gripped, a tensile load of about 10 lbs was applied and the anti-buckling guide was installed for those tests that had compression cycles. These steps were carried out with the load frame operating in displacement control with the load protect safety enabled. The load protect safety prevented the load frame from applying loads of more than +/- 112 lbs. to the specimen. The attachment screws were tightened to the point where the anti-buckling guide could still move, this corresponded to the bolts torqued to finger tight.

Once the anti-buckling guide was properly installed, the load protect safety was disabled, the system was switched into load control mode, and the specimen was loaded to the mid-point of the load cycle. The waveform for the test cycle was also pro-

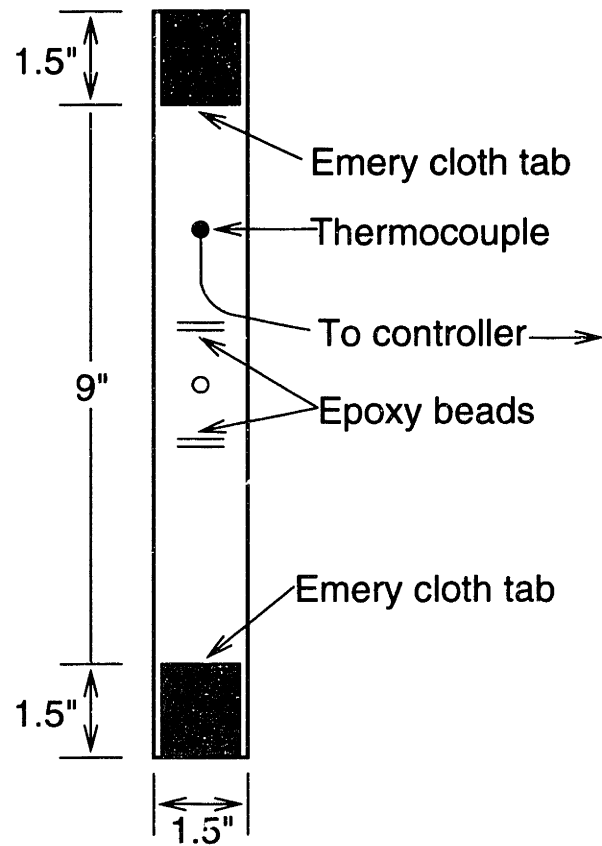


Figure 3-18: Specimen lay out

grammed into the test machine. As a safety precaution, limits were set on the 8500+ controller for both maximum/minimum load and maximum/minimum displacement. The temperature cabinet was placed around the specimen and anti-buckling guide assembly with fiberglass insulation placed in the cracks and openings in the cabinet. The heat gun and the temperature controller were turned on and the assembly was allowed to heat up to the test temperature of 350° F.

For tests where the extensometer was used to monitor damage accumulation, it was installed and calibrated with the specimen being held near zero load. Since the clip gauge was built by Instron, it was automatically recognized by the 8500+ controller and the auto-calibration routine was used. Once the specimen was at the midpoint load and still at room temperature, an initial slow ramp was performed to ensure that the clip gauge was functioning as expected. The ramp used was Instron's havertriangle curve at 0.015 Hz. The havertriangle consists of a single ramp up to the maximum load (in this case, from the midpoint of the cyclic load) and a single ramp back to the original point. A sketch of the havertriangle waveform and the cyclic waveform are shown in Figure 3-19.

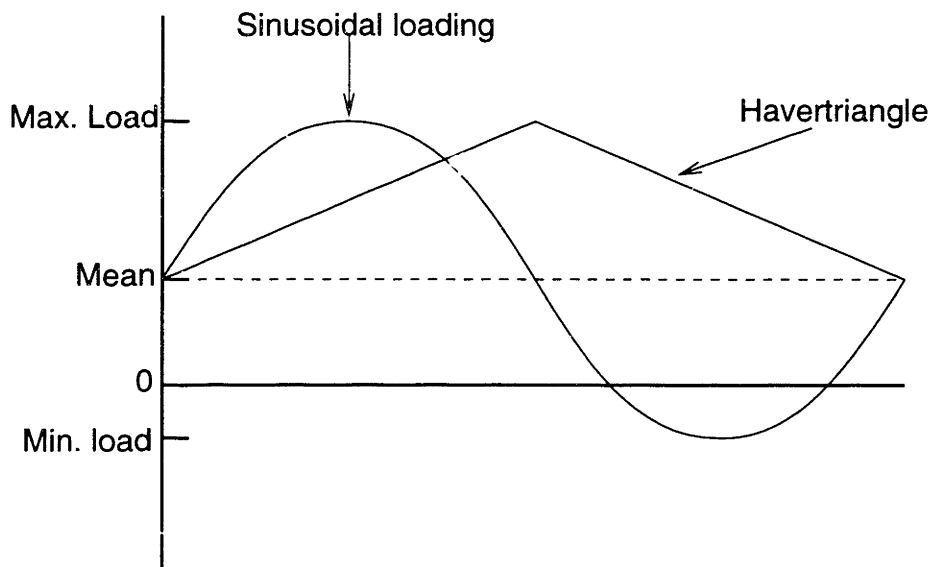


Figure 3-19: Cyclic waveforms

During the cyclic portion of the tests, data could not be collected from the exten-

someter. In order to collect stiffness data, the cycling was stopped and the specimen was ramped for one cycle to the maximum load for that test. The frequency of the cycle was 0.015 Hz. After the stiffness data had been collected, the fatigue cycling was restarted. A load profile for a section of the TiGr tests is shown in Figure 3-20. Stiffness data was taken at approximate logarithmic intervals (i.e. 1000, 2000, 5000, 10,000, etc.).

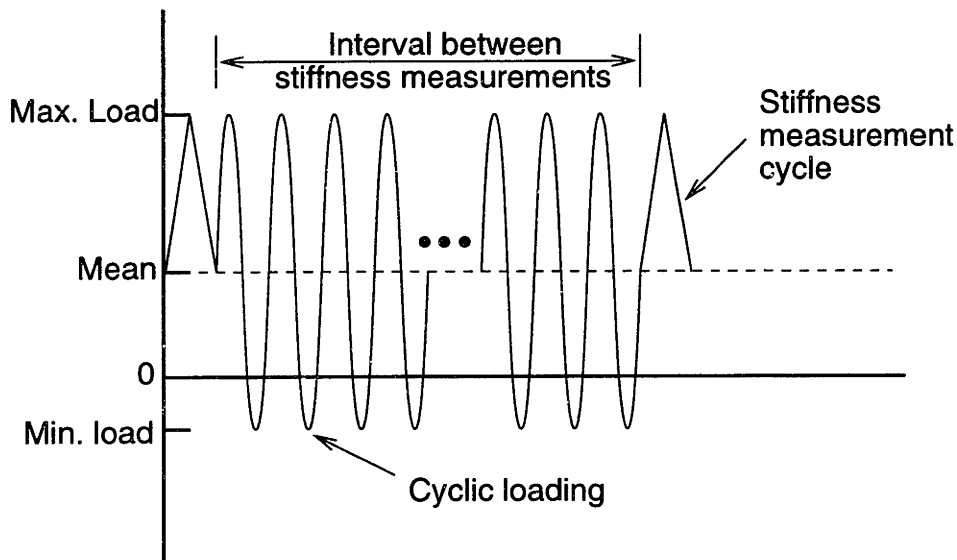


Figure 3-20: Load profile for TiGr test

The waveform chosen for stiffness measurements was arbitrary. In order to confirm that the choice of the load range for stiffness measurement did not affect the data, a comparison of two different stiffness measurement cycles was made. The specimen was ramped twice, once from the mean load and once from zero. The non-dimensional stiffness was monitored for both sets of data and the results are presented in Figure 3-21. The data shows no significant change in the stiffness reduction between the two ramp methods. Therefore, the rest of the testing was done using the ramp from the mean stress.

In tests where residual tensile strength was measured, cycling was stopped either at a desired cycle count or at a certain stiffness loss. The extensometer was removed from the specimen and the oven was reheated to the test temperature. After reaching

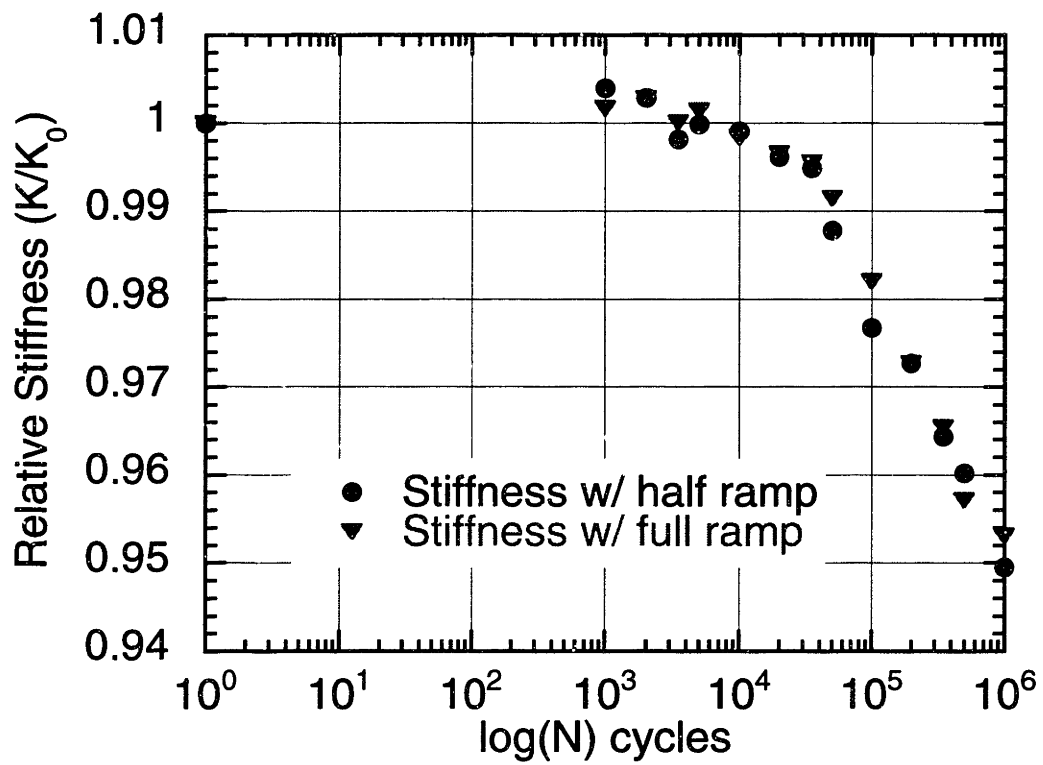


Figure 3-21: Comparison between stiffness measurements for two load ranges

the test temperature, the specimen was loaded to failure in displacement control using a single ramp at 0.099 inches per minute.

3.4 Polishing and Microscopy

An extensive program of polishing and microscopy was carried out to track damage accumulation in the test specimens. In polymer matrix composites X-Ray radiography is often used to monitor damage accumulation. However, the presence of a metal facesheet precludes the use of such techniques.

Each specimen in this part of the test program was sectioned using a diamond grit saw blade on a milling machine. The specimens were cut to approximately $5/8"$ x $5/8"$ as shown in Figure 3-22. Figure 3-22 also indicates the surface of interest for each piece. In sections 3, 4, and 5 the surface perpendicular to the loading direction was viewed while in sections 6 and 7 the edge parallel to the loading direction was observed. Each section was marked along its edge in $1/16"$ increments as reference points during grinding.

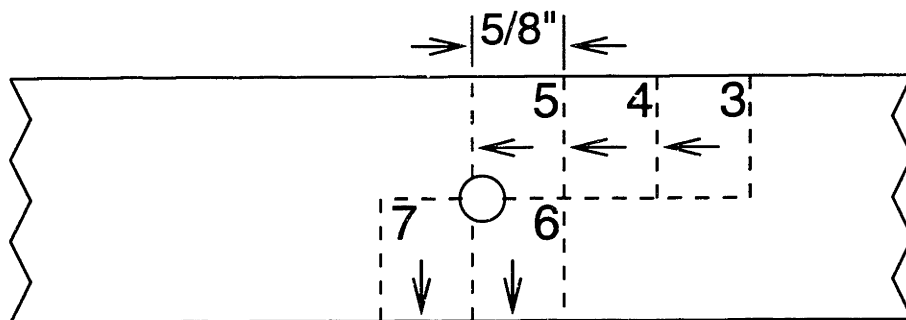


Figure 3-22: Specimen section diagram

After the specimens were sectioned, they were potted in a two part epoxy. The epoxy consisted of 15 grams of Epo-kwick resin mixed with 3 grams of Epo-kwick hardener. The mixture was poured over the section in a 1 inch diameter Buehler Sampl-kup. The plastic mold was pretreated with Buehler Release Agent to allow for

Table 3.2: Polishing sequence (approximate)

Grit size (microns)	Time (min.)
30	45
15	50
9	20
6	35
3	30
1	35

ease in removing the potted section.

The polishing was performed using a Buehler Ecomet IV polishing system. Initial grinding was performed with a grinding wheel with water as the lubricant. Once the initial layer was ground to the desired level, the surface was polished using a Buehler 12" polishing cloth with Buehler METADI II Diamond polishing compound. Buehler Automet Lapping Oil was used as the lubricant. Table 3.2 shows the approximate polishing schedule to grind 1/16" from the specimen. Between each size of polishing grit, isopropyl alcohol was used to thoroughly clean debris from the surfaces so the next wheel did not become contaminated.

When the surfaces were polished to one micrometer, the specimens were examined and photographed using an optical microscope. Pictures were taken of the damaged regions using Polaroid Type 55 film. The pictures were used to characterize the damage at that depth. The specimens were then ground down further to observe the damage at the next level. After a 5/16" depth of grinding, the specimens were too short for the sample holder. These specimens were back filled with more epoxy to allow further observations.

Chapter 4

Experimental Results

The experimental results are presented in three sections. The first gives the results of the Open Hole Tension (OHT) tests. The second section describes the damage progression in the laminates. The third section presents the results of the fatigue tests and describes the failure mechanisms.

4.1 Open Hole Tension Tests

Open hole tension tests were performed to establish a baseline for the fatigue tests. The specimens were tested at 350° F, with the anti-buckling guide installed. The tests were run in displacement control using a single ramp at a loading rate of 0.099 inches per minute. Table 4.1 lists the failure loads of the OHT tests.

The OHT strength used as a baseline for the rest of the test program was the average of the four OHT test results. Tests three and four were conducted on specimens from the second batch of material provided by Boeing. Figure 4-1 shows the load vs. strain for the third OHT test. The strain data was taken with the extensometer, so the strain represents the deflection over the gauge length (50 mm) normalized by the gauge length of the extensometer. The load vs. strain curve was linear until just before final fracture.

Table 4.1: Open hole tension test results

Test #	OHT strength (lbs)
1	12,430*
2	12,940
3	11,200†
4	11,060†

* Specimen slipped in grip at 11,560 lbs. Grip pressure was increased and specimen was reloaded to failure.

† Specimens tested were from the second batch, series 1469-15

The fracture surface in the OHT tests after failure was clean as compared to the fatigue failures. Figure 4-2 is a picture of an OHT specimen after failure. The fibers broke at approximately the centerline on both sides of the hole and little or no delamination was present as opposed to the fatigue failures where significant delamination existed and the fracture surfaces were much more fibrous.

4.2 Damage Progression

For homogeneous materials, such as most structural metals, fatigue failure is generally the result of a single crack propagating until it reaches a critical size at which point fast fracture occurs. In most composite materials, and hybrid laminates in particular, the fatigue response is more complicated. In hybrid laminates, there are many damage modes present which interact to cause failure. This section of the test program was designed to characterize the damage modes in notched TiGr specimens and to determine at what point in the test cycle the damage formed and how the damage modes interacted.

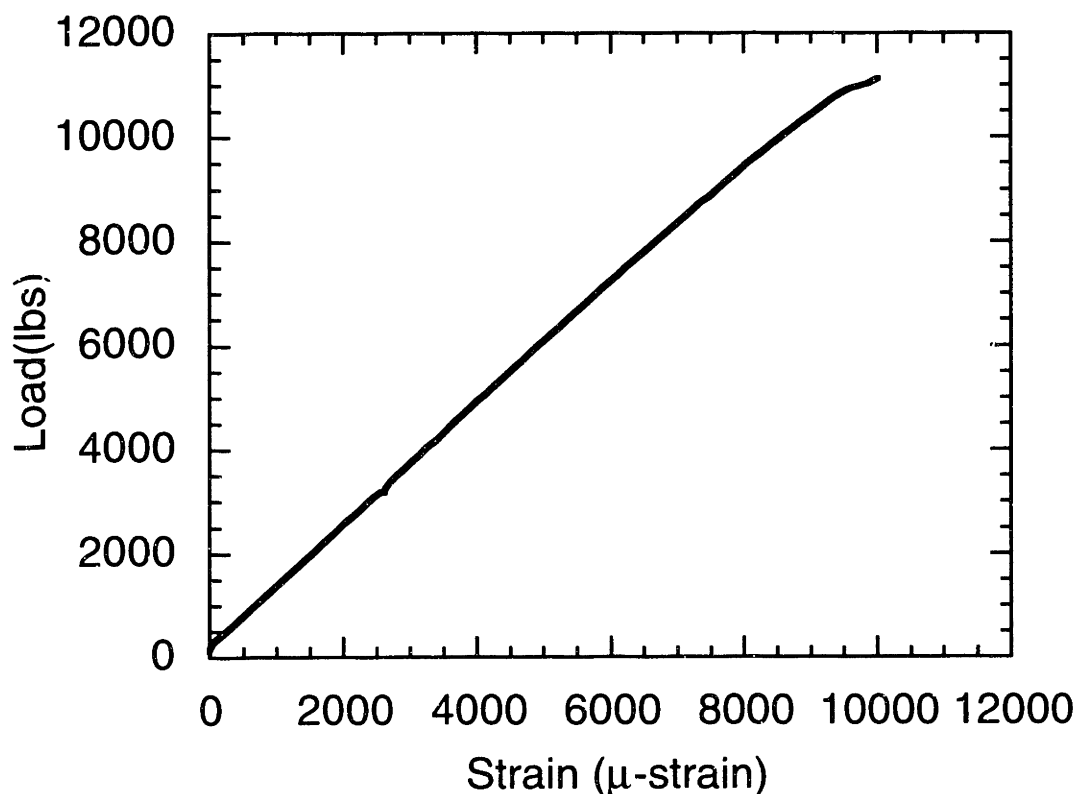


Figure 4-1: Load vs. strain for OHT test 3

4.2.1 Damage modes

The first damage types visible to the naked eye are titanium facesheet cracks. In the TiGr laminates tested, the facesheet ligaments that were cracked had either one or two cracks which had propagated from the hole to the specimen edge. Figure 4-3 shows an example of the two facesheet crack patterns observed during testing. The presence of two cracks propagating completely to the specimen edge is significant. In monolithic materials, multiple cracks may initiate at the edge of the hole, but only one will propagate completely across the ligament. The two crack pattern in the TiGr tests indicate that the underlying PMC plies transmit load across the cracked ligament, which allows a second crack to advance to the specimen edge.

In order to view the damage below the surface, the specimens were sectioned, potted in epoxy, polished with diamond grit down to one micrometer, and viewed under an optical microscope as described in Section 3.4. With this procedure it was

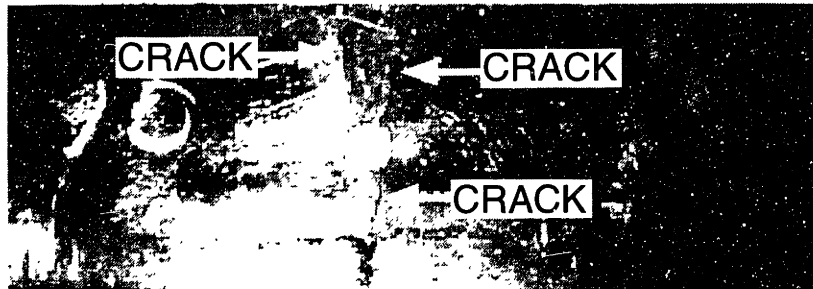


Figure 4-3: Facesheet crack pattern

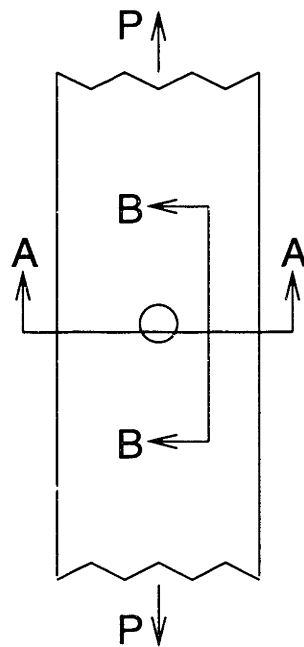


Figure 4-4: Cross-section schematic for micrographs

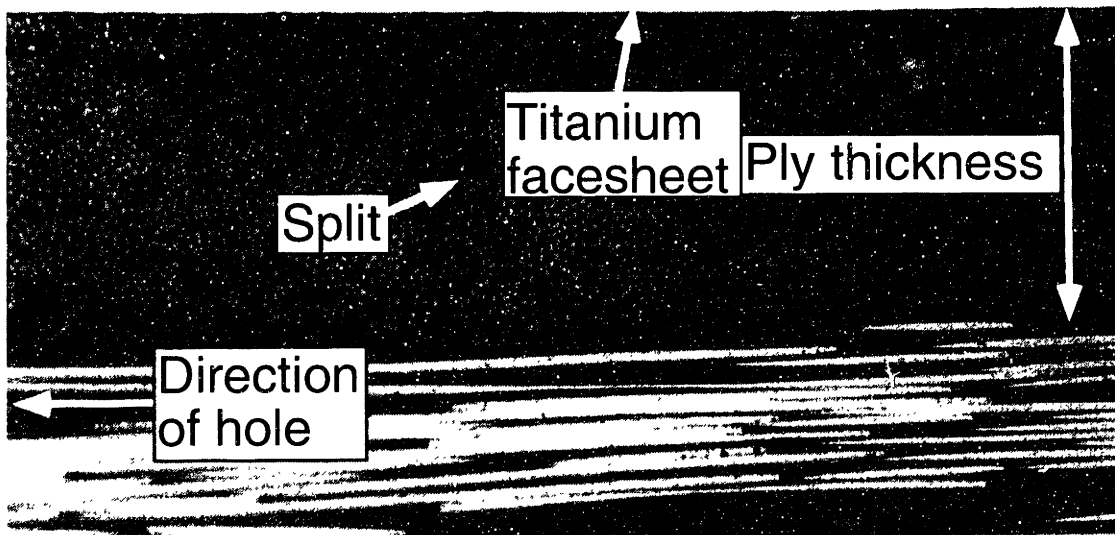


Figure 4-5: Micrograph of titanium delamination in the outer ply

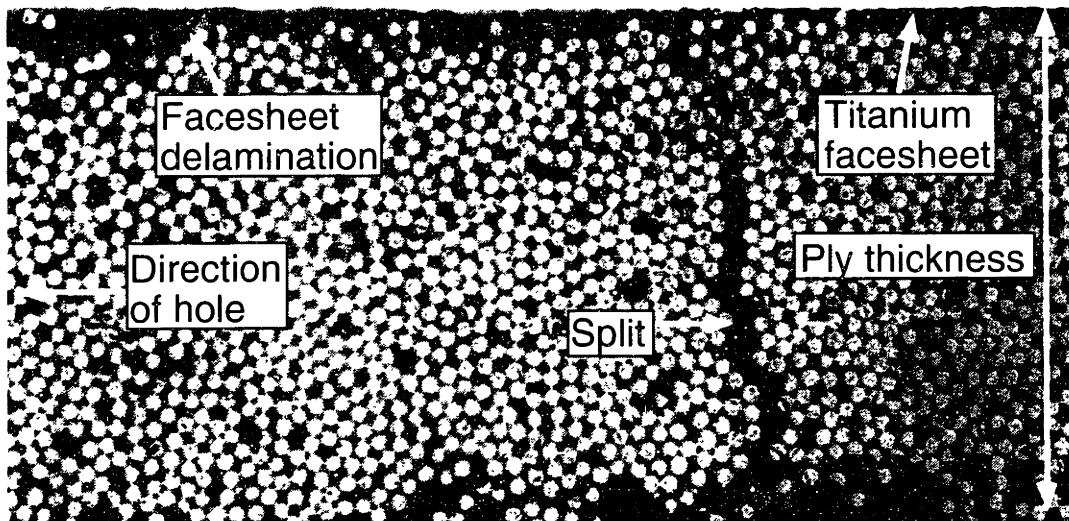


Figure 4-6: Micrograph of titanium delamination in the outer ply

in the laminate such as delamination and undoubtedly contributes to the overall reduction in stiffness.

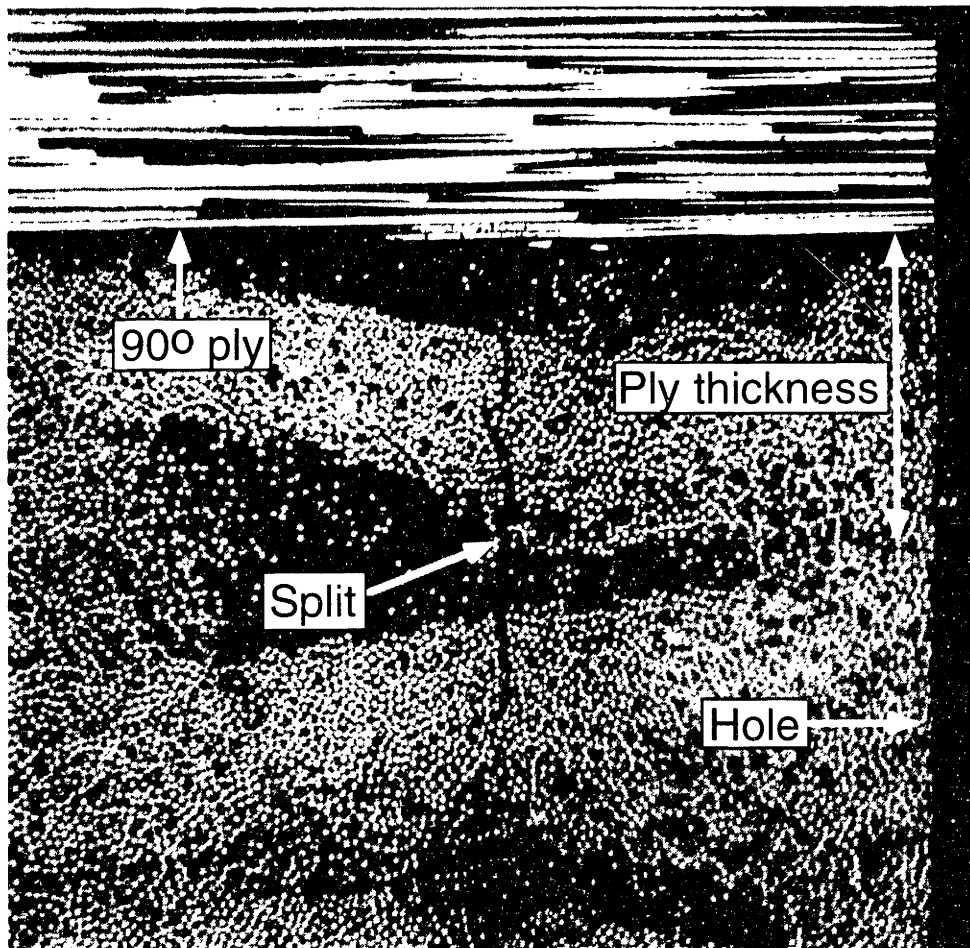


Figure 4-7: Micrograph of 0° ply splitting

The third type of damage that occurs in the PMC laminate is ply cracking in the 90° plies, perpendicular to the applied load. Figure 4-8 is an example of this type of damage, taken on section BB. The density of the ply cracks appears to increase with increased cycles, although this was not determined quantitatively.

4.2.2 Damage mapping

To obtain a qualitative picture of how damage in hybrid laminates develops, a series of experiments was performed in which specimens were cycled to a predetermined num-

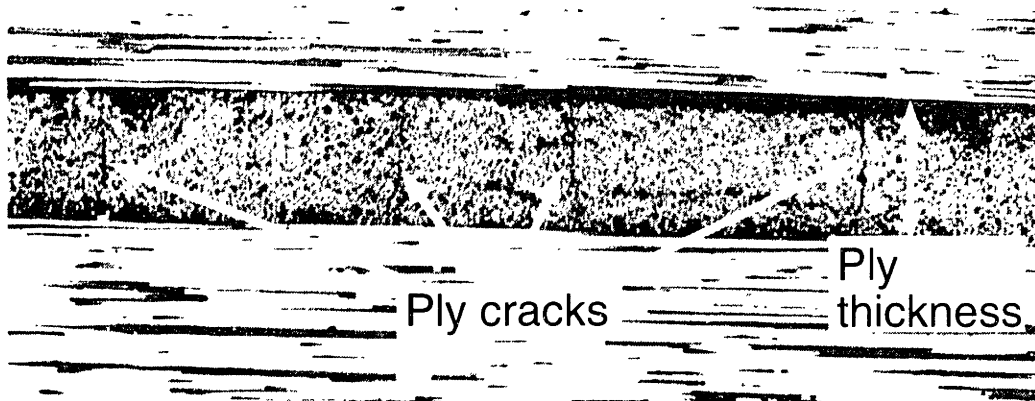


Figure 4-8: Micrograph of 90° ply cracks

ber of cycles and then polished and observed under a microscope. Tests were run to 1,000, 10,000, 30,000, and 100,000 cycles. This series of tests was performed at 350° F, $R = 0.1$ (as opposed to $R = -0.2$), due to an extra ply (i.e. a lay-up of $[Ti/0_2/90/0_4/90/0/Ti]_t$) in the specimens cycled to 1,000, 10,000, and 100,000 cycles, which would have resulted in buckling had the specimens been loaded in compression. It should be noted that the schematics of the damage were drawn by examining the damage in a single quadrant and assuming a symmetric damage state.

A plot of stiffness drop as a function of number cycles for the four tests is shown in Figure 4-9. These measurements and the observations of damage permit a correlation to be made between the stiffness loss and the damage state.

The damage in the 1000 cycle specimen is shown in Figure 4-10. At this cycle count, the damage was very limited. On the surface, no facesheet cracks were visible. Ply splitting tangential to the hole, similar to that shown in Figures 4-5, 4-6, 4-7, appears in the 0° plies. Limited delamination between the facesheet and the PMC core was evident between the two ply splits in the vicinity of the hole. Ply cracking (Figure 4-8) in the 90° plies perpendicular to the applied load also appeared in the region near the hole. These cracks were only evident in the region between the ply splits.

At 10,000 cycles, the damage was significantly more extensive as shown schem-

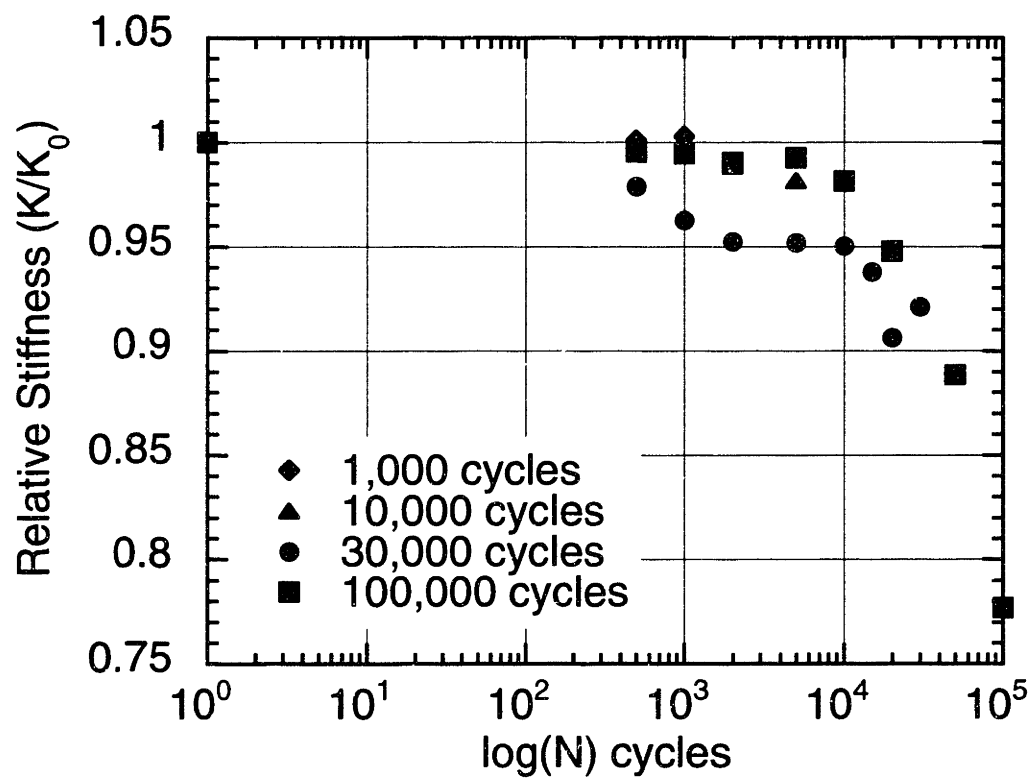


Figure 4-9: Stiffness loss for damage progression specimens

atically in Figure 4-11. The ply splits had extended well beyond the radius of the hole and the delamination between the facesheet and the core filled most of the area between the splits. On the outside edge of the splits, delamination between the 0° plies and the 90° plies had begun to appear. The density of the ply cracking was higher than the 1,000 cycle specimen. However, the length of the ply cracks was still small and the cracks were restricted to the regions between the ply splits and the specimen edges. No visible signs of facesheet cracks were observed at this level of cycling.

After 30,000 cycles the titanium facesheet cracks extended one third of the way across the facesheet ligaments. In general, the damage state appeared to be less extensive than the 10,000 cycle specimen. The ply splits in this specimen did not appear to extend as far as in the 10,000 cycles specimen, and the ply cracks did not appear to be as dense. The main difference from the 10,000 cycle specimen is the appearance of facesheet cracks. Cracks extended from the hole edge in four places on the front and the back. Additional ply splits, similar to those seen in the 100,000 cycle specimen also appeared outside the original splits tangential to the hole. One explanation for the change in damage state from what was expected might be that the lay-up for the 30,000 cycle specimen was slightly different than the lay-up of the other three experiments. The 30,000 cycle specimen did not have the extra 0° ply in the lay-up. A sketch of the damage after 30,000 cycles is shown in Figure 4-12.

A sketch of the damage state after 100,000 cycles is shown in Figure 4-13. At 100,000 cycles, the titanium cracks had propagated completely across the specimen and the facesheets had begun to peel back from the PMC core. The original ply splits had grown longer and additional splits formed away from the hole region. Delamination between the 0° and the 90° plies appeared to initiate around these new splits. Both the density and the extent of the transverse ply cracking increased in the 100,000 cycle specimen. The region near the specimen edge showed a large increase in the length of the ply cracks. By contrast, the area near the hole showed only a small increase in the number and length of ply cracks.

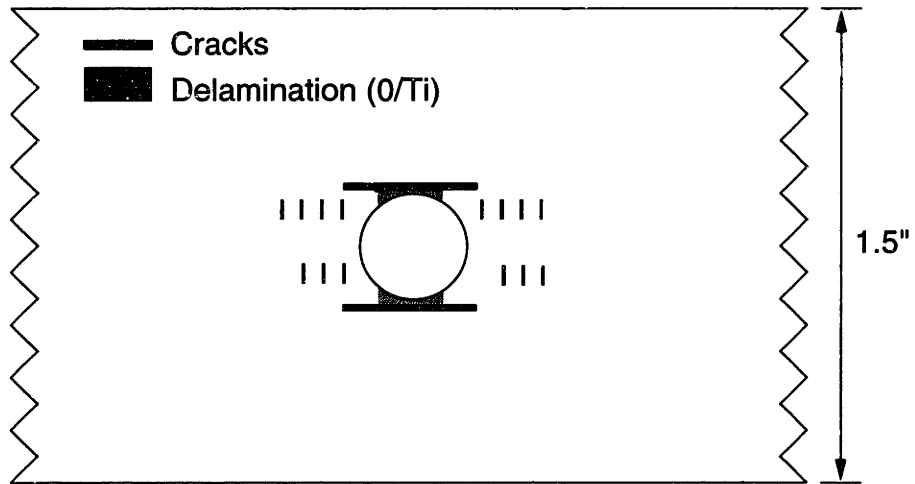


Figure 4-10: Sketch of damage after 1,000 cycles

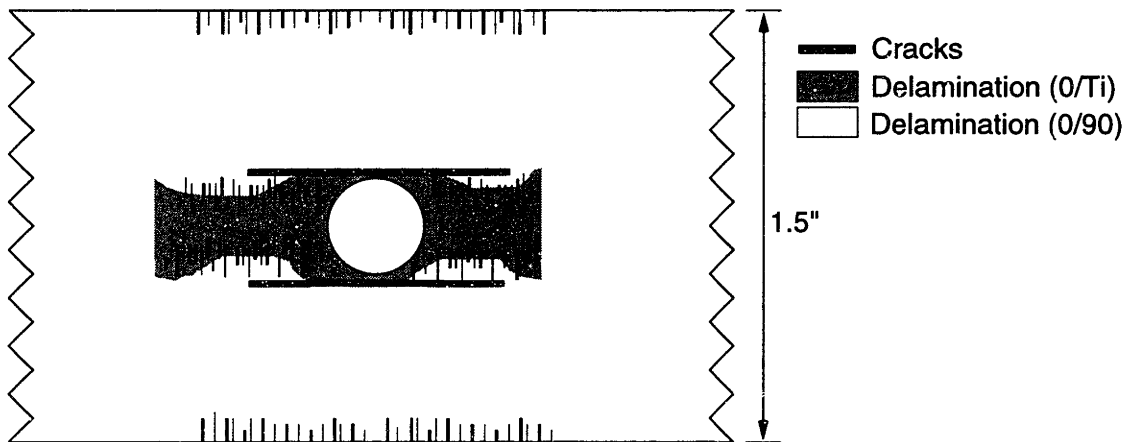


Figure 4-11: Sketch of damage after 10,000 cycles

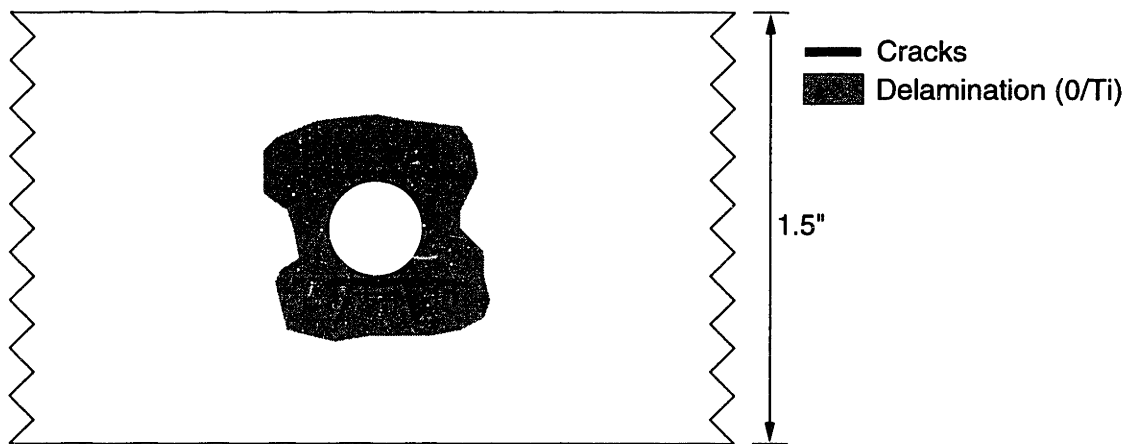


Figure 4-12: Sketch of damage after 30,000 cycles

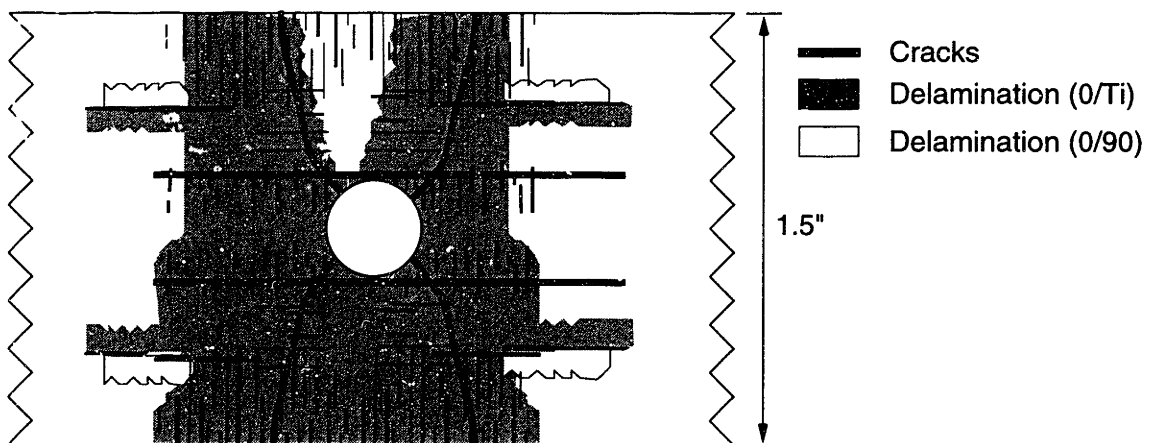


Figure 4-13: Sketch of damage after 100,000 cycles

4.3 Fatigue Tests

4.3.1 Failure mechanisms

Unlike most homogeneous materials, a precise definition of fatigue failure, in the sense of an S-N curve, does not exist for TiGr. During the initial testing, two different practical definitions of failure were used as end points for the fatigue tests. One was complete fracture of the specimen and the other was extensive delamination.

At intermediate load levels, between 30% and 45% OHT strength, the tests were stopped when the extensive delamination caused the specimen to wedge in the anti-buckling guide. Delamination was present at the interfaces between the titanium facesheet and the 0° plies as well as at the interface between the 0° plies and the 90° plies. The delamination at the Ti/ 0° interface was mainly present near the hole, while away from the hole, the delamination was principally at the $0^\circ/90^\circ$ ply interface. A sketch of the damage state is shown in Figure 4-14.

At the highest cyclic stress levels tested (i.e. approximately 60% OHT strength) specimen failure occurred when the specimen fractured into two pieces. However, the specimen was able to carry a small load after failure, due to the friction of fiber pull-out.

The extremely fibrous fracture surface reflects the extensive subcritical damage and contrasts with the cleaner fracture surface of the OHT specimens (Figure 4-2). On one side of the hole, the fibers fractured near the grip. On the other side, the fibers broke near the hole. A plan view photograph of one of the specimens tested at this load level is shown in Figure 4-15 and a side view showing the extensive delamination is shown in Figure 4-17. A schematic of the failure is also included as Figure 4-16 and Figure 4-18 shows a close-up of the fractured specimen in the region near the hole.

Significant delamination was also present in the failed specimen. The Ti/ 0° interface was delaminated near the hole and the Ti foil was peeled back towards the grip. It is important to note that some of the fibers, both 0° and 90° , remained attached to the facesheet after delamination further indicating a good bond between the titanium

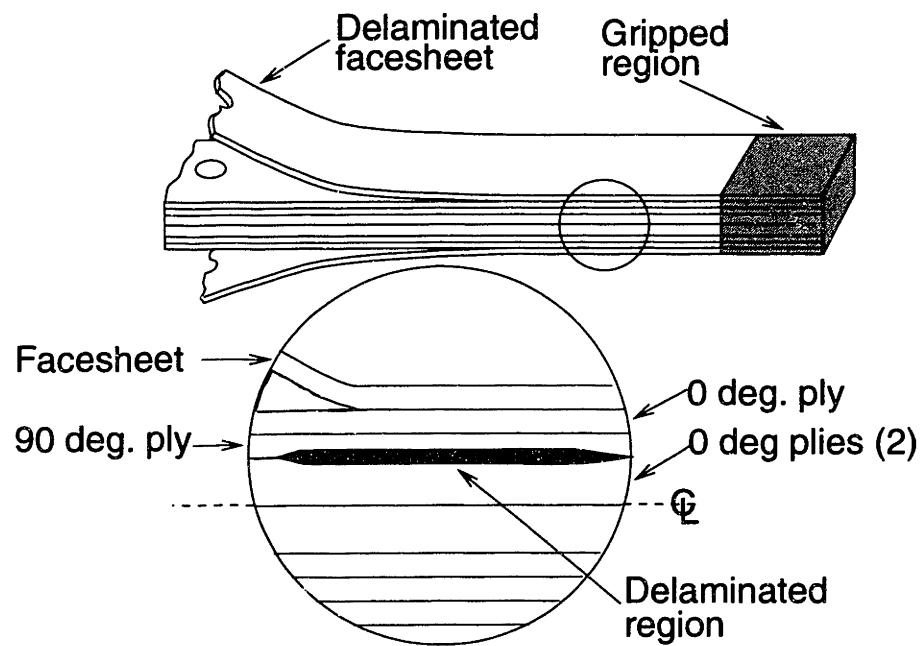


Figure 4-14: Sketch of damage in delaminated specimen

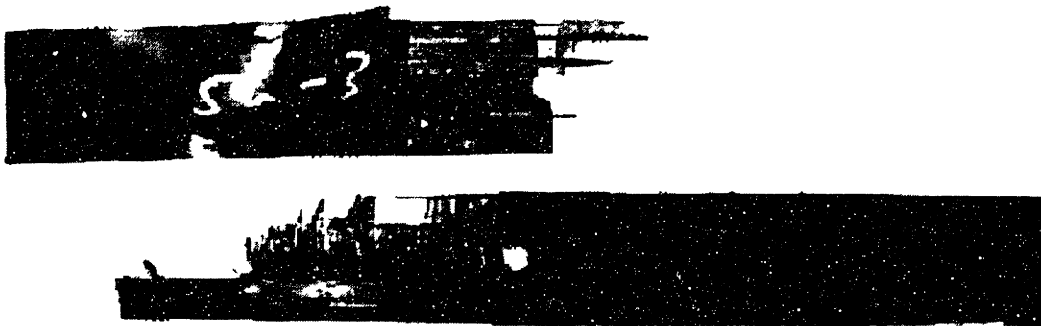


Figure 4-15: Front view of specimen that failed via fracture

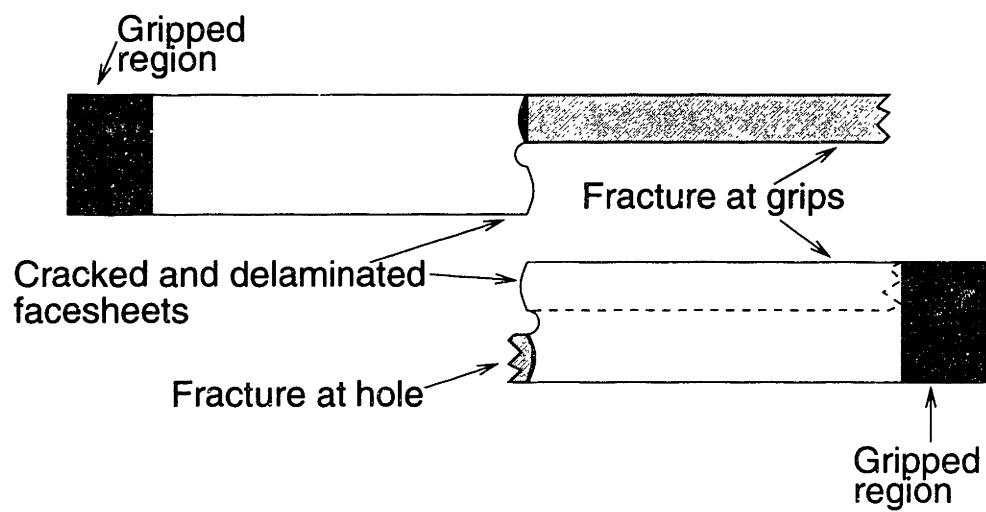


Figure 4-16: Schematic of fracture failure

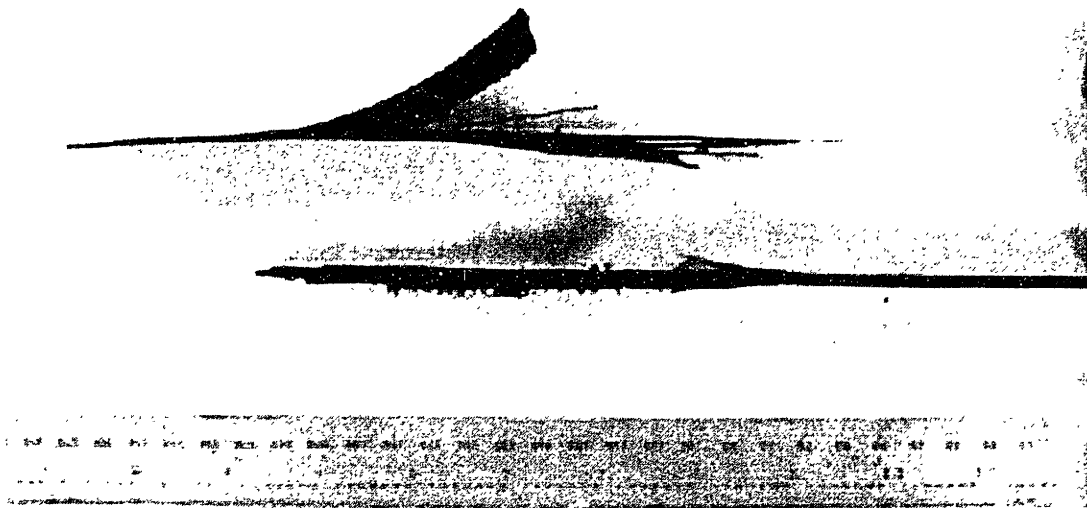


Figure 4-17: Side view of specimen that failed via fracture



Figure 4-18: Damage region near hole after failure via fracture

facesheets and the PMC core. The 90° ply was delaminated from the 0° ply at both the inner and outer interfaces. It is not clear where the delamination originated. The 90° ply was also severely cracked and frayed in the failed specimen as shown in Figure 4-18.

4.3.2 Fatigue life results

In order to provide an unambiguous comparison of damage states with which to construct S-N type diagrams, a series of tests were conducted in which 50% stiffness reduction was arbitrarily defined as “failure”. This corresponded to a damage state where the titanium facesheets were completely cracked and the delamination had propagated on the order of one inch away from the hole. In most of the specimens the delamination length was greater at the edge of the specimen than in the center of the specimen. A plot of maximum cyclic stress vs. cycles to “failure” is shown in Figure 4-19. Both the 50% stiffness data and the data from the delamination and fracture failures is included in the plot. Figure 4-20 shows the relative stiffness vs. cycles for the tests cycled to 50% stiffness loss.

Although only one test to 50% stiffness reduction was performed at each load level, the fatigue life results are consistent. On the semilog plot, the 50% reduction in stiffness failure points are approximately linear.

4.3.3 Residual strength tests

In tests that used stiffness reduction as an end point for cycling, residual tensile strength tests were performed on the fatigued specimens. Residual strength as a function of stiffness loss is plotted in Figure 4-21. No clear trends emerged from the small number of tests that were conducted. Most of the tests showed little or no loss in strength and no correlation with the stiffness loss.

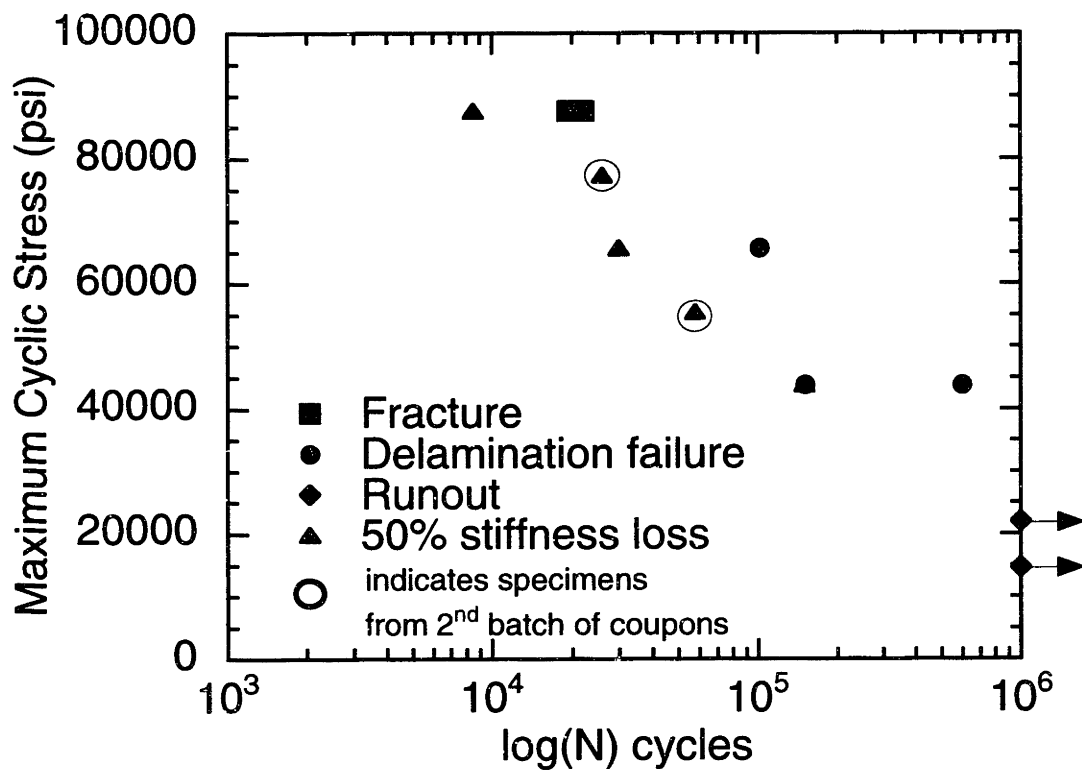


Figure 4-19: Fatigue life data for TiGr 2-6-2

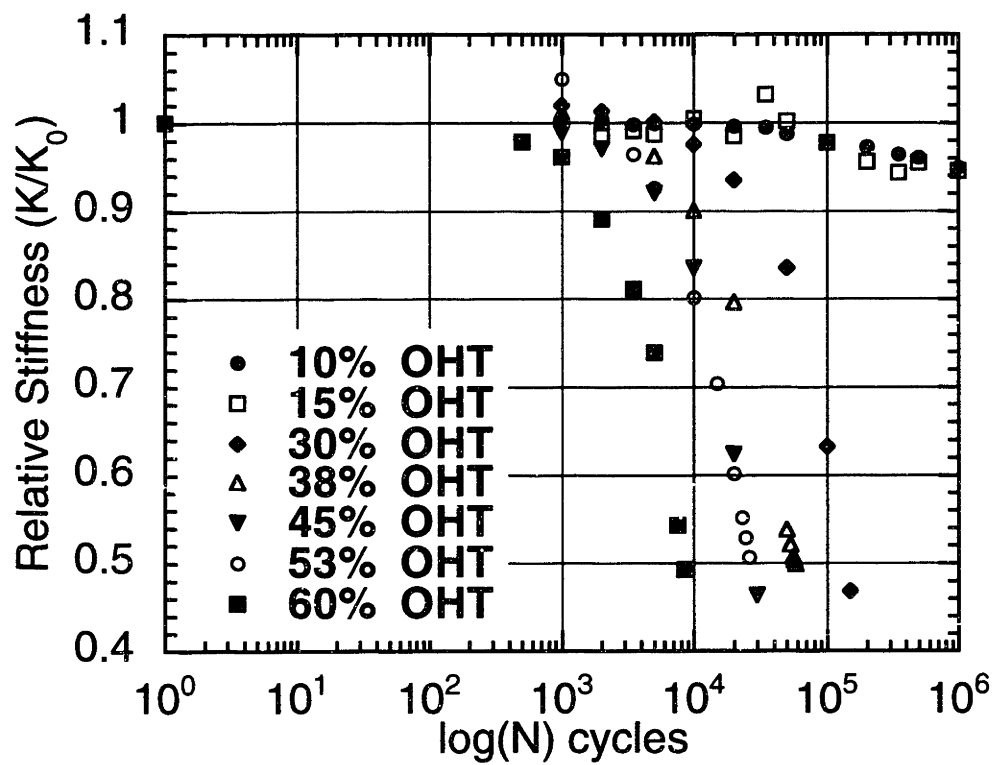


Figure 4-20: Stiffness vs. cycles at seven stress levels

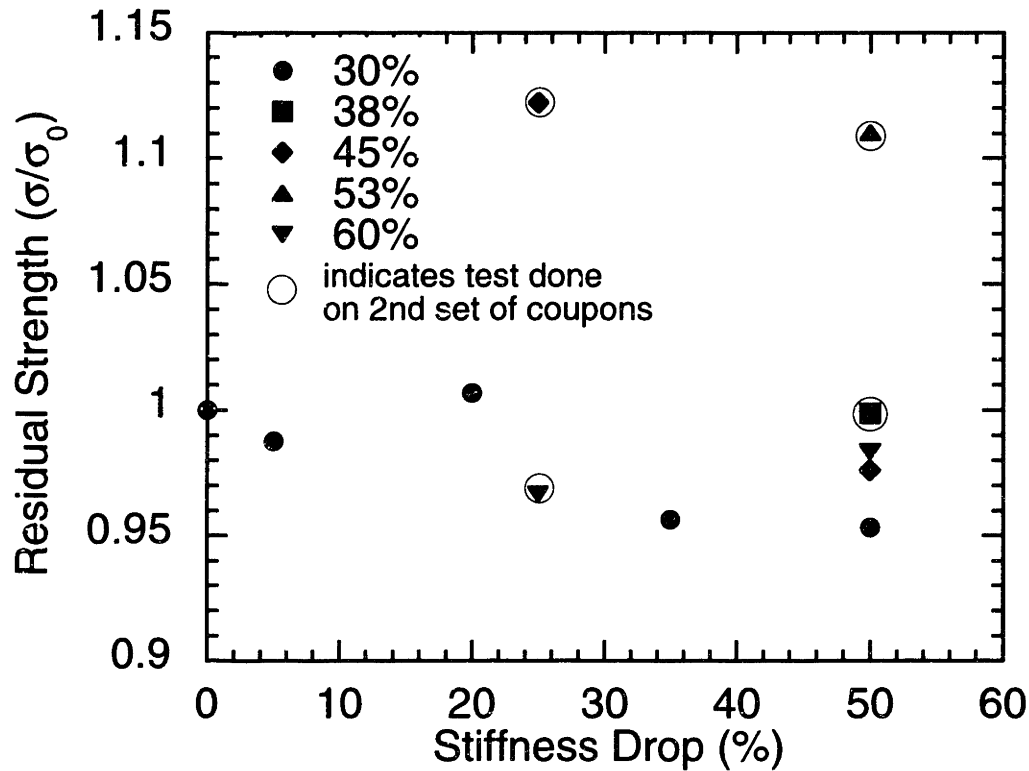


Figure 4-21: Residual strength vs. stiffness loss

4.4 Room temperature test

For comparative purposes, one fatigue test was conducted at room temperature at 30% of the OHT strength with $R=-0.2$. The stiffness loss vs. number of cycles is shown in in Figure 4-22. The number of cycles to reach 50% reduction in stiffness is almost an order of magnitude higher for the room temperature environment. This indicates that the rate of damage accumulation is much higher in the high temperature environment. Since it is believed that the main cause of the stiffness loss is delamination, this suggests that the rate of delamination is increased due to the high temperature.

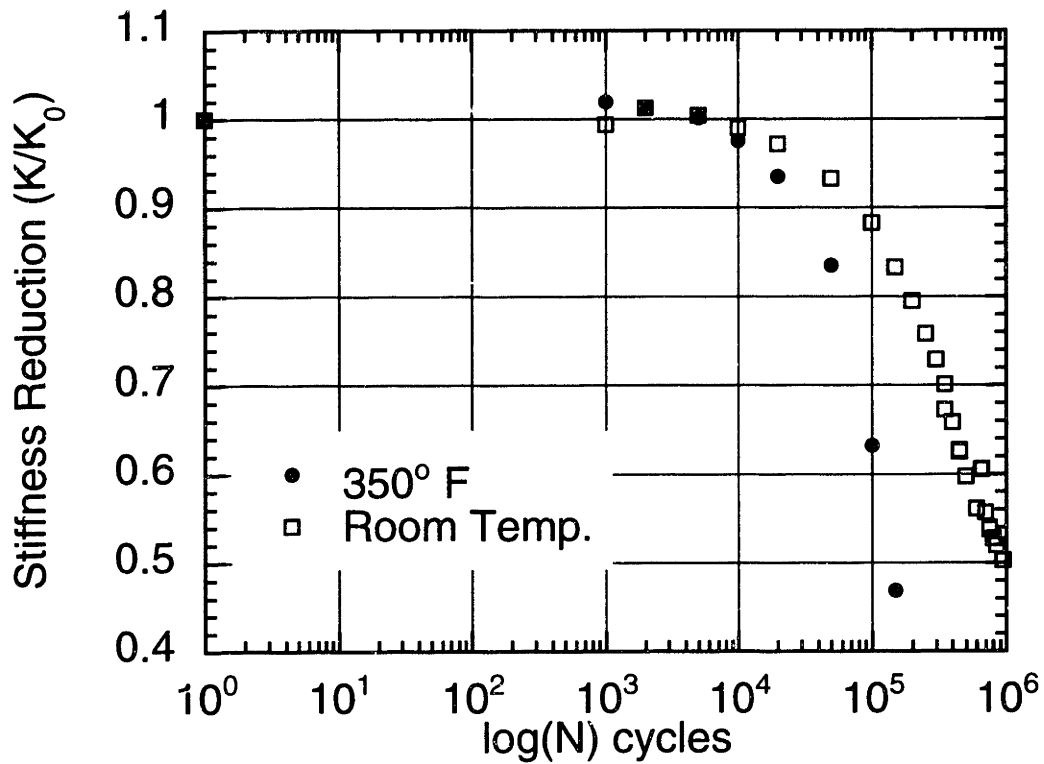


Figure 4-22: Stiffness loss vs. cycles at room temperature (30% OHT, $R=-0.2$) and 350° F

4.5 Summary

The key damage mechanisms leading to failure were determined to be cracking of the titanium facesheets, delamination of the facesheets, delamination of the composite plies, ply splits in the 0° plies, and transverse ply cracks in the 90° plies. These damage modes interact with each other and can lead to complete failure by fracture or a functional failure due to extensive delamination and the associated stiffness loss.

Chapter 5

Discussion

The analyses presented in this chapter are a first order treatment of the damage modes observed in the TiGr laminates tested during this project. The analyses suggest that although many complex, interacting, damage mechanisms occur during fatigue testing, they are generally consistent with the damage mechanisms observed in monolithic titanium or pure PMC composites. The analyses also provide insight into the governing parameters of each of the damage modes which will help guide future material development.

5.1 Facesheet Cracking

The first visible form of damage was cracking of the titanium facesheets. Since one of the purposes of using a metal facesheet is to protect the PMC core, cracking of the facesheets is undesirable. In this section, a first order analysis is conducted to better understand the factors contributing to the initiation of such cracks. There are assumed to be two principal contributions to facesheet cracking, the local stress concentration and the titanium S-N behavior.

5.1.1 Stress concentration

When a notch is introduced into a structure, the stress is concentrated around the notch. This stress concentration is a prime location for the nucleation of cracks. The stress concentration factor, K_t , is defined as the local stress near the notch tip divided by the remote stress (Equation 5.1) [20].

$$K_t = \frac{\sigma_{max}}{\sigma_{\infty}} \quad (5.1)$$

In this research, the notch is a circular hole in the center of the specimen. For an isotropic material with a centrally located circular hole in an infinite plate, the stress concentration factor is three [37]. However, for an anisotropic material such as TiGr, the stress concentration is also a function of the degree of anisotropy in the material. Figure 5-1 shows the stress distribution in the region near the 0.25” hole in a TiGr specimen. The calculation is made using work by Bishop [38]. The maximum stress concentration factor for this particular TiGr lay-up is 4.6. The result is only an approximation since the calculation does not include a correction for the finite width of the TiGr samples. For comparison, Figure 5-2 shows the corresponding plot for an isotropic material. The plots were produced using the MATLAB analysis software. The source code is included in Appendix A.

5.1.2 Titanium fatigue cracks

Figure 5-3 shows S-N data for Ti 15-3-3-3 cycled at 400° F, with $R = 0.1$ and $K_t = 3$, taken from an article by Fanning [39]. S-N data is used for comparison to crack initiation data in the titanium facesheets because of the assumption that the number of cycles needed to initiate a crack constitutes a majority of the fatigue life. Once the crack has initiated, only a small fraction of total life remains.

The data points are divided into two clusters, one at around 30,000 cycles (open markers) and the other at 10^7 cycles (filled markers). The open markers represent failed specimens and the filled markers represent specimens that cycled to the run-out

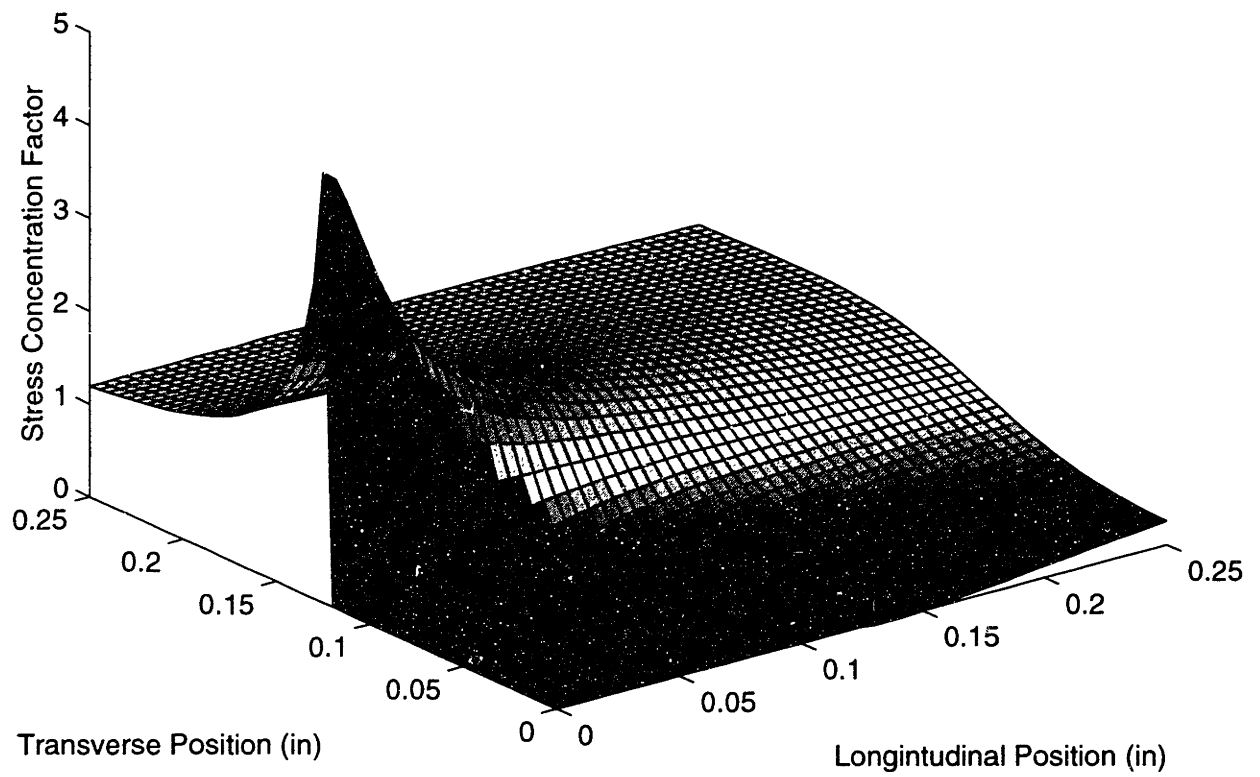


Figure 5-1: Stress concentration in notched TiGr 2-6-2

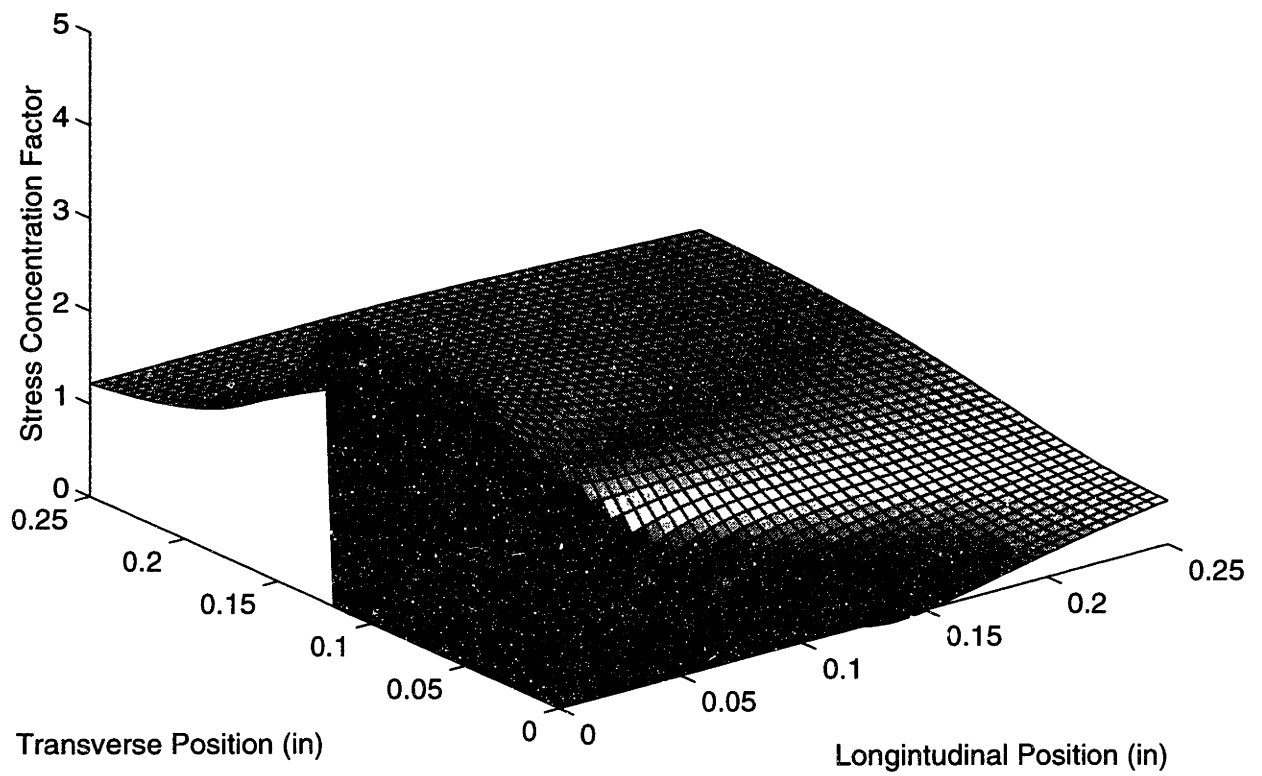


Figure 5-2: Stress concentration for an isotropic sample

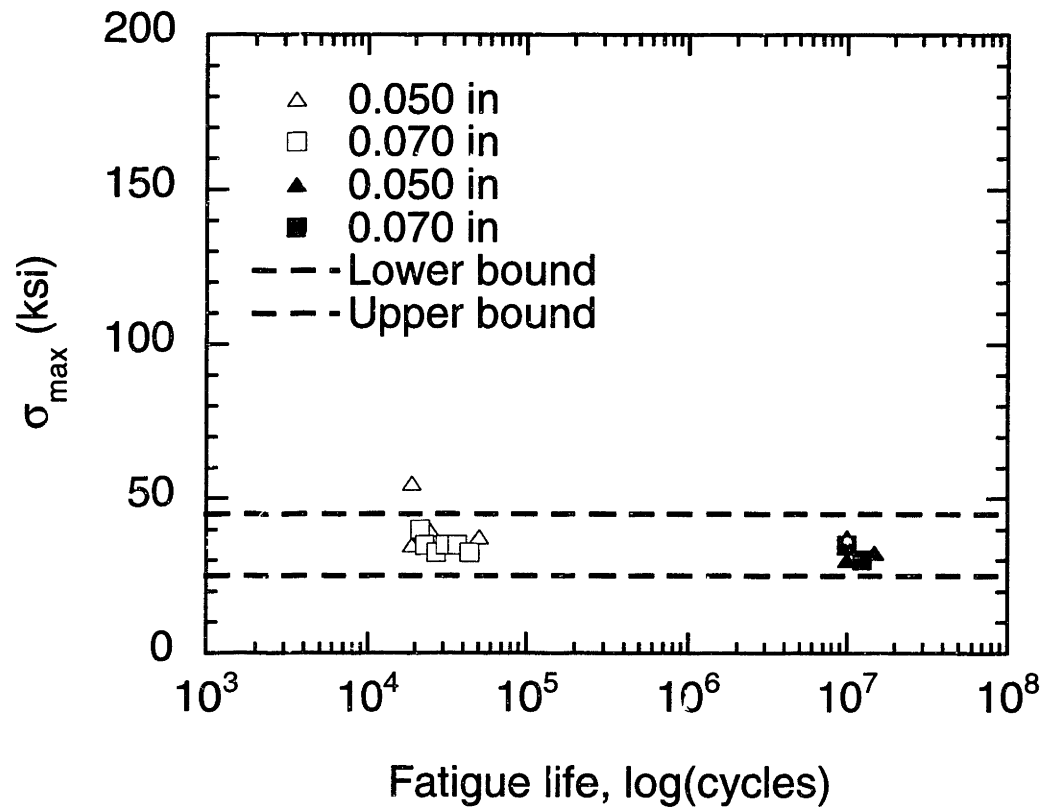


Figure 5-3: S-N data for titanium 15-3-3-3, $K_t = 3$, 400° F [39]

point without failure. Two lines are drawn on the plot approximating an upper and lower bound for failure stress for the titanium.

By itself, the titanium fatigue data does not describe the behavior of the facesheets in TiGr. The stress values from Figure 5-3 need to be weighted for the differences between monolithic titanium sheets and facesheets of TiGr laminates. Weighting factors were introduced for the difference in Young's moduli and the difference in stress concentration factors as shown in Equation 5.2. The weighted stress boundaries in terms of applied far field gross stress in the laminate are shown in Figure 5-4 along with data for first facesheet crack observed during fatigue cycling. The difference in R-ratio was not accounted for in the comparison. Another beta titanium alloy, Ti-13V-11Cr-3Al, shows decreasing life with decreasing R-ratio for a constant maximum stress.

$$\sigma_{TiGr} = \sigma_{Ti} * \frac{E_{TiGr}}{E_{Ti}} * \frac{K_{t,Ti}}{K_{t,TiGr}} \quad (5.2)$$

where:

σ_i = applied stress

E_i = Young's modulus

$K_{t,i}$ = stress concentration factor

The enclosed temperature cabinet made it impossible to directly observe the cycle count at crack initiation. The open squares with left-pointing arrows in Figure 5-4 indicate the cycle count at which the first crack was visually observed. The open diamond with a right-pointing arrow indicates that one specimen had no noticeable facesheet cracks when the test was stopped after 10^6 cycles. The observations were made when the cycling was interrupted and indicate an upper bound for first crack data. Only once was the test stopped at a point where the crack had just nucleated at a macroscopic level.

It is important to note in Figure 5-4 that for the tests at 44 ksi, 66 ksi, and 86 ksi (30%, 45%, and 60% OHT strength), the stress levels are above the upper bound for titanium fatigue failure. Therefore, the fatigue cracks that appear in the titanium

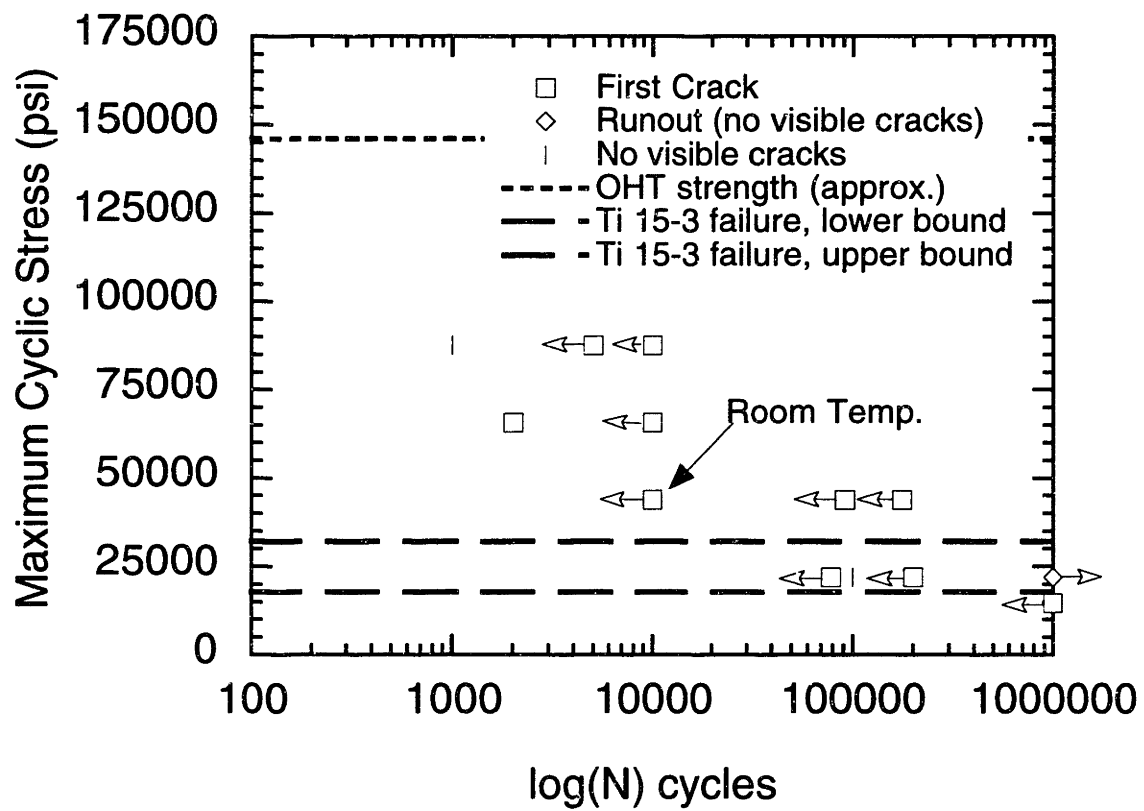


Figure 5-4: First crack data for TiGr 2-6-2

facesheets are consistent with the behavior of monolithic Ti 15-3-3-3 at these *in-situ* stress levels. For tests run at 15% OHT strength, the maximum stress falls between the two stress boundary lines. In two of the tests, facesheet cracks appeared, while for the third no cracks were visible. This is consistent with the behavior for 15-3-3-3 titanium where some of the tests failed at the stress levels between the bounds, while others did not fail.

In the test at 10% OHT strength, a single crack formed in each ligament on one side of the specimen and had propagated partially across the ligament. The stress level was below the projected lower bound for Ti 15-3 and therefore no cracking was expected. However, the TiGr tests had a lower R-ratio than the data for monolithic titanium ($R = -0.2$ vs. $R = 0.1$). Based on the assumption that fatigue life in monolithic titanium decreases with decreasing R-ratio, the predicted lower bound may be higher than the actual lower bound would be for $R = -0.2$.

5.1.3 Crack growth

Previous research on ARALL laminates indicate that the crack growth rate of the facesheet cracks slows down as the crack grows and that eventually the crack growth may stop. This behavior was noticed in experiments by Toi and Fujiwara [5] and by Papakyriacou et al. [8]. This type of retardation does not occur in metals, where the crack growth rate generally increases with increasing crack length.

The retardation effect comes from the delamination and other damage mechanisms that grow along with the crack as well as the crack bridging provided by the 0° plies. Figure 5-5 illustrates two cases: case 1 where delamination is growing radially with a crack that has not yet reached the specimen edge and case 2 where the facesheet crack has propagated to the edge of the specimen and the delamination is growing away from the crack. For case 1, the increase in delamination area goes as the square of the length as the crack propagates a unit length da . As the crack grows, it requires an increasing amount of energy to sustain the propagation, proportional to the current crack length. If the amount of energy required to grow the crack and the

accompanying surface is greater than the available energy, crack growth will cease. In case 2, the delamination area grows linearly with da . The amount of energy to create a new delamination surface is independent of the delamination length as the delamination propagates. Once the crack has reached the edge and the facesheet has started to peel back, it will continue to propagate with each load cycle.

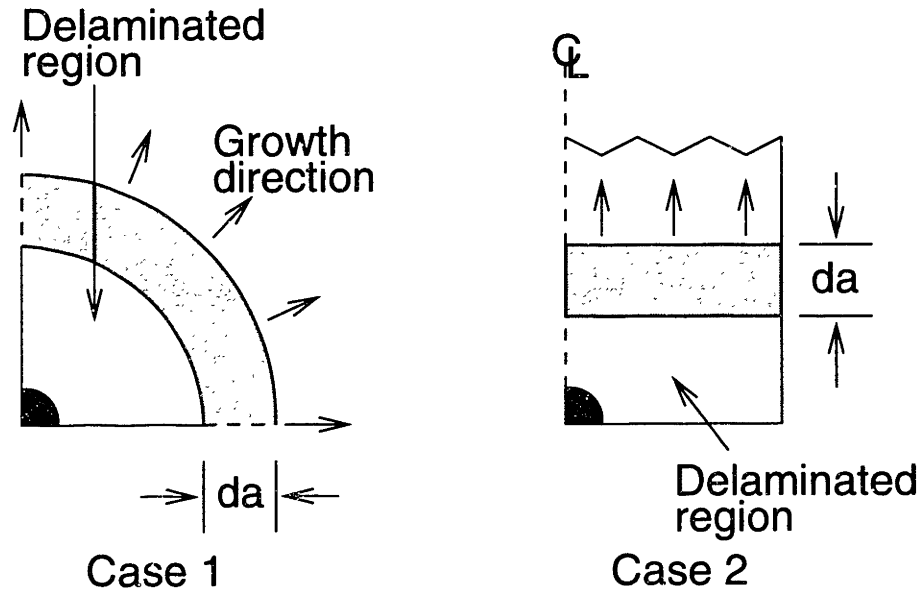


Figure 5-5: Schematic of delamination growth

The test specimens used in this study were too narrow to capture the decrease in crack growth rate. Wider specimens need to be tested in order to capture the decrease in crack growth rate effects, in addition an *in-situ* crack monitoring capability is required.

5.2 0° Ply Splitting

Ply splits in the 0° plies were one of the first damage modes observed in the PMC core. The splits formed parallel to the loading axis and tangential to the hole. A micrograph of ply splitting in TiGr is shown in Figure 4-7. Just as fatigue cracks in the facesheets were consistent with Ti 15-3 behavior, ply splitting is consistent with the behavior of

notched 0/90 cross-ply PMC laminates. Figure 5-6 shows an X-Ray of ply splitting in a cross-ply AS4/PEEK laminate [40].

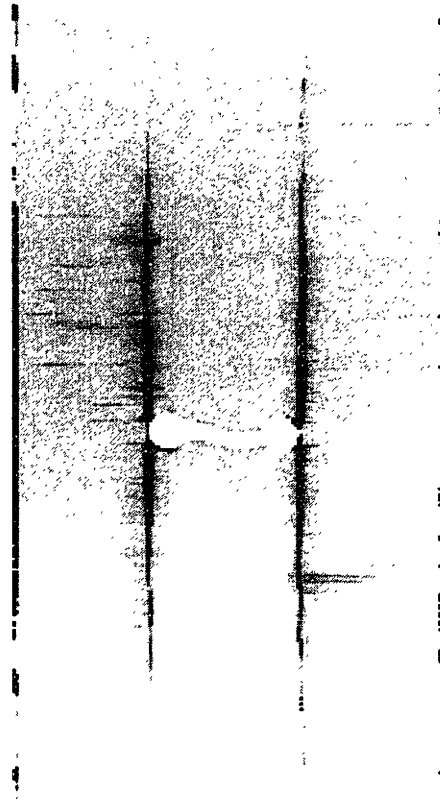


Figure 5-6: X-Ray of damage in 24 mm wide, AS4/PEEK cross-ply laminate [40]

In the micrograph, the dark vertical lines are splits, similar to those observed in the TiGr. Also visible are small ply cracks in the 90° plies and some delamination. The splits initiated at the holes and grew as the number of cycles increased. Figure 5-7 shows a plot of the half split length, l , normalized by the notch size, a , vs. cycles for two load levels. The curve at 300 MPa (43.5 ksi) in Figure 5-7 has a stress level similar to the TiGr tests run at 30% OHT strength, the load level at which the damage progression studies were conducted.

The micrographs of the TiGr cross sections summarized in the damage sketches (Figures 4-10, 4-11, 4-12, 4-13) provided qualitative information on split growth. The measured split lengths are plotted in Figure 5-7 with the data for AS4/PEEK. The

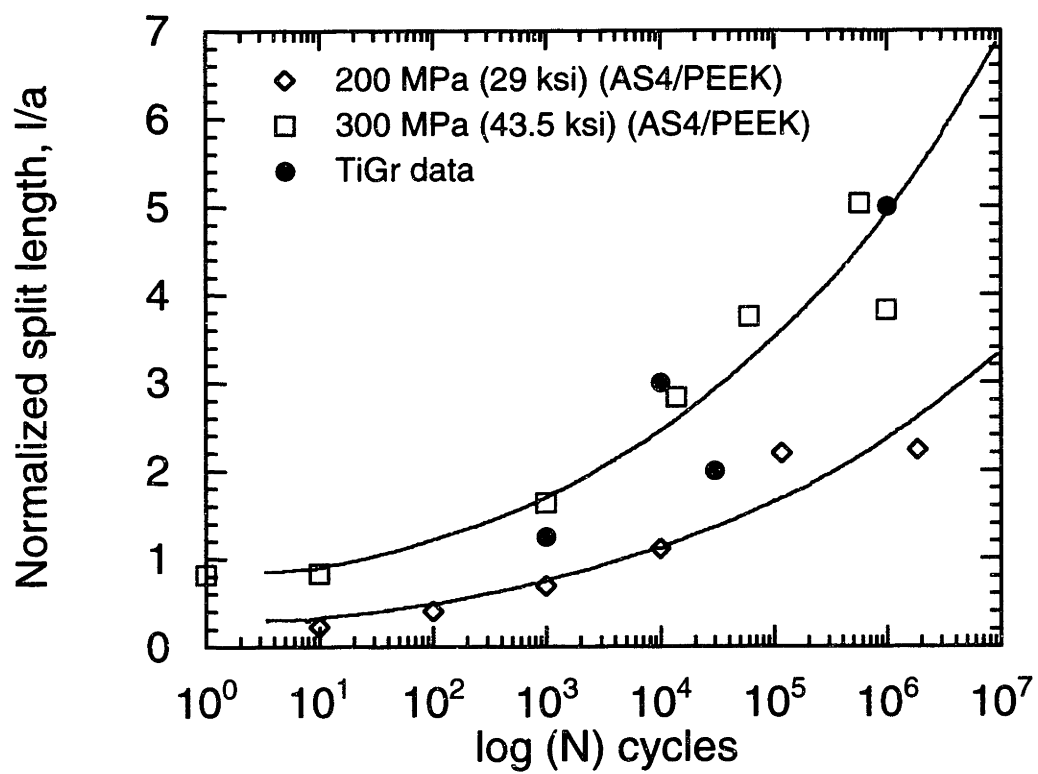


Figure 5-7: Split length vs. cycles in AS4/PEEK cross-ply laminate [40]

tests at 10^3 , 10^4 , and 10^5 cycles were conducted at 51 ksi and the 30,000 cycle specimen was conducted at 45 ksi. The difference is a result of the extra ply in the first three specimens. All the tests were conducted with a maximum stress level of 30% OHT strength as described in Section 4.2.2. The split length in the TiGr tests correlate well with the data for AS4/PEEK showing that on a qualitative level, the split lengths in the PMC core of TiGr are similar to the damage observed in other cross-ply, fiber-thermoplastic composite systems.

In general, any sort of damage in the composite is undesirable. However, the ply splits can be beneficial. As the ply splits grow they blunt out the stress concentration due to the notch in the PMC plies. This leads to an increase in residual strength for notched specimens. The other damage that grows along with the splits, e.g. delamination and ply cracks, may also cause the split to stop growing after reaching a certain length. At this point, the amount of energy needed to grow the split and the associated damage region is less than the available energy, similar to the phenomenon governing growth of titanium facesheet cracks.

5.3 Strain Energy Release Rate

The delamination of the facesheets was modeled using an energy approach based in linear elastic fracture mechanics. The strain energy stored in the specimen was calculated for a control volume in front of and behind the delamination front, as shown in Figure 5-8.

The difference between the two calculated strain energy release rates ($G = dU/dA$) is the amount of energy available to propagate the delamination. If the available energy is greater than the energy required to create new delamination surface then the delamination will propagate. A similar approach has been applied to splitting in wood [41].

$$\frac{dU}{dA} = \left(\frac{dU}{dA}\right)_{core} - \left(\frac{dU}{dA}\right)_{laminar} \quad (5.3)$$

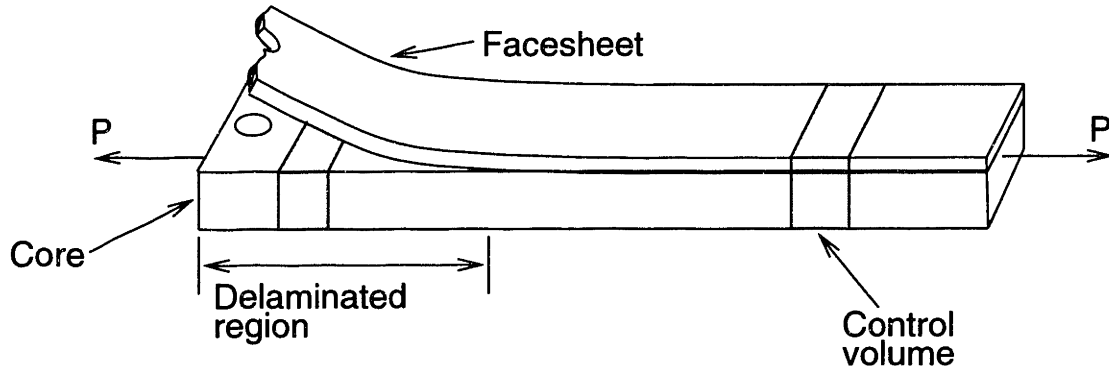


Figure 5-8: Schematic of strain energy release rate calculation

$$\left(\frac{dU}{dA}\right)_{core} = \frac{1}{2} * E_{core} * \left[\frac{P}{W * t_{core}}\right]^2 * t_{core} \quad (5.4)$$

$$\left(\frac{dU}{dA}\right)_{laminar} = \frac{1}{2} * E_{face} * \left[\frac{P_{face}}{W * t_{face}}\right]^2 * t_{face} + \frac{1}{2} * E_{core} * \left[\frac{P_{core}}{W * t_{core}}\right]^2 * t_{core} \quad (5.5)$$

$$P_{face} = \frac{P}{1 + \frac{W * t_{core} * E_{core}}{W * t_{face} * E_{face}}} \quad (5.6)$$

$$P_{core} = \frac{P}{1 + \frac{W * t_{face} * E_{face}}{W * t_{core} * E_{core}}} \quad (5.7)$$

where:

E_{core} = core stiffness (from CLPT)

t_{core} = core thickness

E_{face} = facesheet stiffness

t_{face} = facesheet thickness

W = specimen width

Using the above equations, a comparison was made between several facesheet materials to compare their propensities to delaminate. Table 5.1 gives the properties

Table 5.1: Material properties for strain energy release rate comparison

Material	E (Msi)
Titanium 15-3-3-3	16.3 [30]
2024 Aluminum	10 [42]
Quasi-Isotropic PMC	8.8 [30]
90° PMC	1.0 [30]

for the different engineering materials and Figure 5-9 presents the results. The core lay-up was maintained as $[0/90/0_2]_s$ for all four facesheet materials, which is the same as the core in the TiGr samples studied in this project. Equation 5.5 implies that the delamination strain energy release rate (SERR) scales with the facesheet modulus. Thus, out of the four materials plotted, titanium has the highest SERR curve. The calculation was performed using MATLAB, and the code is included in Appendix A.

The influence of a relatively high SERR for titanium facesheets is likely to be amplified by the fatigue delamination response of the Ti/PMC interface. Delamination growth rate, da/dN , is often found to be a function of the change in strain energy release rate with the form $da/dn \propto (\Delta G)^{\frac{m}{2}}$ (i.e. similar to the Paris Law for metals). The exponent, m , is typically between 8 and 10 for delamination in polymer matrix composites, thus a small increase in ΔG leads to a large increase in delamination growth rate.

Figure 5-10 is a plot of da/dN vs. ΔG , for the delamination growth in the thermoplastic material APC2, which illustrates the effect of ΔG on the crack growth rate [26].

5.4 Stiffness Reduction

As the facesheet delaminated from the core, the overall stiffness of the specimen was lowered. In order to study this effect, a model was constructed using a series of linear springs to represent the specimen as shown in Figure 5-11. Three damage modes

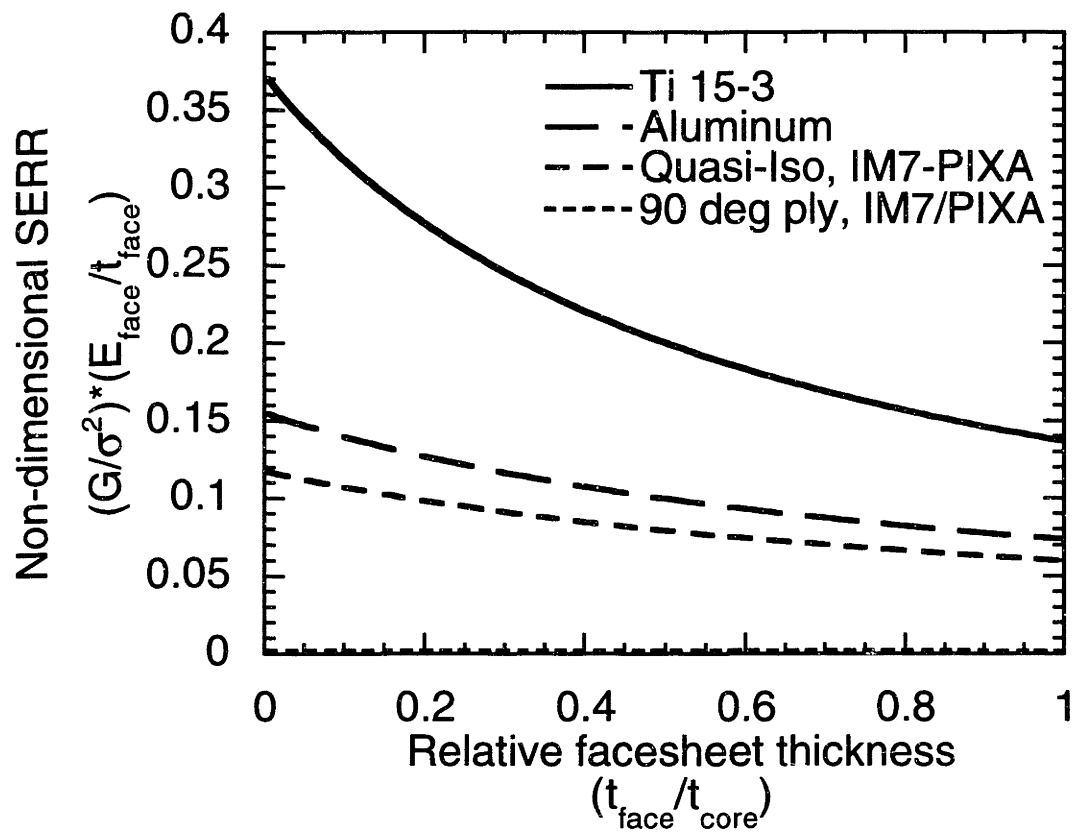


Figure 5-9: Normalized strain energy release rate as a function of relative facesheet thickness for four facesheet materials

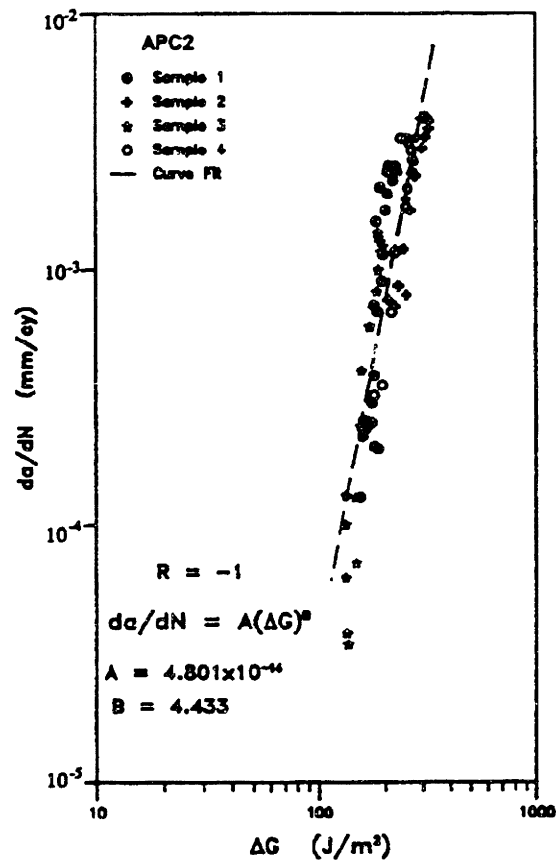


Figure 5-10: Crack growth vs. strain energy release rate amplitude (ΔG) for APC2 [26]

were studied, the case where the titanium facesheet had cracked and delaminated from the PMC core, the case where the strength and stiffness contribution from the 90° plies was eliminated due to damage, and the combination of the first two cases where the facesheet had delaminated and the 90° plies were damaged. For the third case, only the 0° plies can carry load in the damaged region.

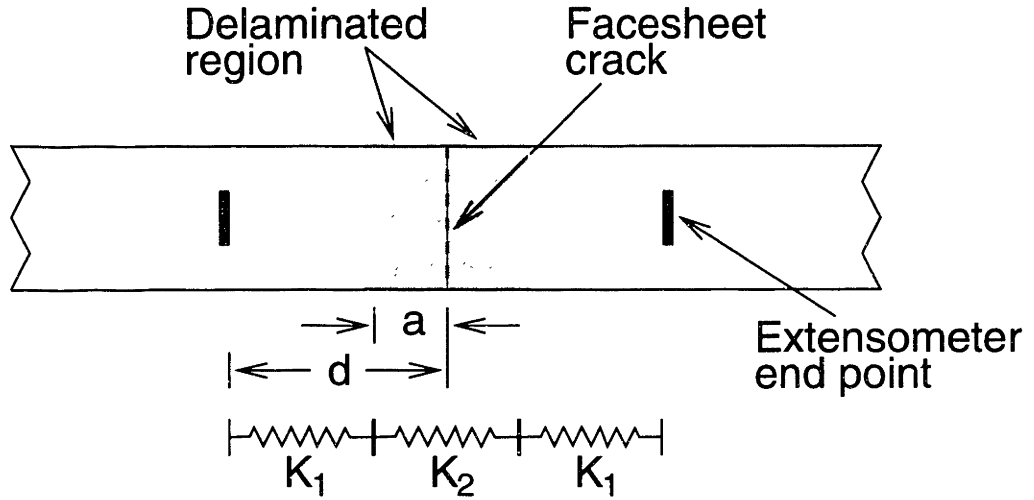


Figure 5-11: Schematic of stiffness model

The model specimen is unnotched with a centrally located facesheet crack. The delaminated region extended a distance, a , away from the facesheet crack in both directions. The stiffness is calculated in a center section over the gauge length of the extensometer. When the damaged zone is smaller than the gauge length, the stiffness is a function of both the damaged and undamaged regions. Once the damaged region has extended beyond the extensometer's gauge length, the measured stiffness is that of the entire damaged region. This is because the extensometer remains attached to the titanium and measures the deflection of the entire delaminated region.

The stiffness of the individual sections is calculated using Equation 5.8. The overall stiffness is given by either Equation 5.9 or 5.10.

$$K_i = \frac{E_i * A_i}{L_i} \quad (5.8)$$

where:

E_i = Young's modulus of section

A_i = area of section

L_i = length of section

$$0 < \frac{a}{d} \leq 1 \qquad \frac{1}{K_{total}} = \frac{2}{K_1} + \frac{1}{K_1} \qquad (5.9)$$

$$1 \leq \frac{a}{d} \qquad K_{total} = K_2 \qquad (5.10)$$

A stiffness loss model was constructed for the case where the 90° plies are discounted, reflecting severe damage accumulation during fatigue loading. This case is modeled in a similar manner to the titanium delamination, with a growing damage zone, a , and a stiffness modeled over the gauge length of the extensometer. The damaged region is modeled using “unlaminated” plate theory with the three ply groups (two outer Ti/0 ply groups and the center 0₄ ply group) modeled as parallel springs.

The third case modeled is essentially a combination of the two previous cases. The titanium facesheets are considered to be cracked and delaminated by a distance a . Simultaneously, the 90° plies are damaged over the same distance a . This leaves only the outer 0° plies and the center 0₄ ply group to carry load within the damaged region. The stiffness in the damaged region is modeled with three parallel springs, one for each of the single 0° plies and one for the 0₄ ply group. As before, the calculated stiffness is a function of the damaged and undamaged regions before the damage length was greater than the extensometer gauge length and only a function of the damaged regions after it had propagated beyond the extensometer.

A plot of stiffness loss vs. damage zone size is shown in Figure 5-12. The most severe stiffness loss occurs when the facesheets cracked and delaminated and the 90° plies become damaged. However, the case for only titanium delamination is

only slightly less severe, showing that the loss of the 90° plies has relatively little effect on the stiffness and that the main contribution to stiffness loss arises from the delamination of the facesheets. The calculations were performed using MATLAB and the source code is included in Appendix A.

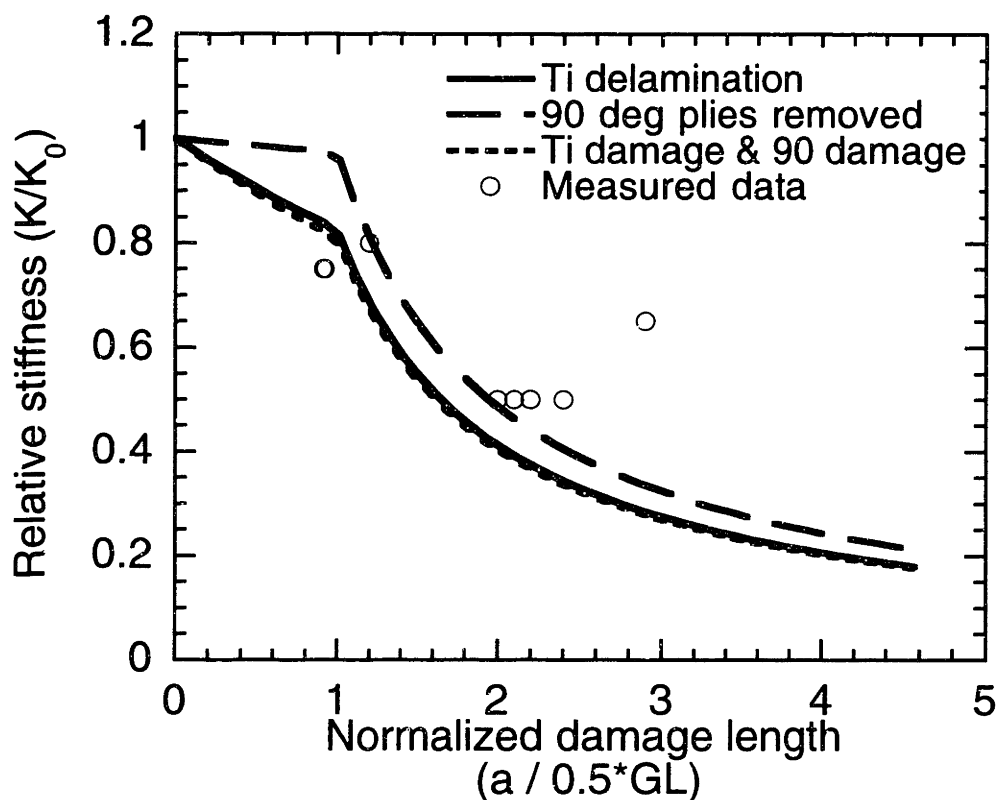


Figure 5-12: Effect of damage on measured stiffness

Figure 5-12 also contains data points of the damage zone size as measured from the fatigue cycled specimens. The data points approximately follow the predicted curve giving some indication that the model is valid as a first order approximation. The damage zone size was not uniform on all sides of the specimen, so the values plotted in Figure 5-12 represents the average damage zone size. The measurements were made assuming that no significant damage growth occurred during the residual strength test.

5.5 Damage Growth Correlation

The above stiffness model was used to relate the measured stiffness data from the 30%, 38%, 45%, 53% and 60% OHT tests to the applied stress levels. The measured stiffness data points (K/K_0), as presented in Figure 4-20, were substituted into the stiffness model to calculate the associated damage zone size, a , thus giving damage zone size as a function of cycles, N . Note that in some of the tests, the stiffness increased slightly for a portion of the cycling. In these cases, where the calculated damage zone was less than zero, the damage zone size was set equal to zero. A second order polynomial regression was performed on the a vs. N data points. Taking the derivative of the polynomial curve fit gives the damage growth rate, da/dN , for the five stress levels. The applied stress levels are presented as ΔG , which is a function of the square of the applied stress. The results are plotted in Figure 5-13 for three different damage zone sizes, $\frac{a}{d}=1.5$, $\frac{a}{d}=1.0$, and $\frac{a}{d}=0.4$. The first value corresponds to approximately a 50% stiffness reduction, the second corresponds to approximately a 25% stiffness reduction and the third corresponds to approximately a 10% stiffness reduction.

When plotted on a logarithmic scale, the calculated values are approximately linear. A power curve of the form $da/dN = C * (\Delta G)^{m/2}$, with $m=3.8$ provides a good fit to the data. This form is similar to that found for the delamination of PMC materials (Figure 5-10), although the exponent, m , is significantly lower. This data reaffirms the belief that delamination is a major contributor to stiffness loss. Further tests need to be performed which measure the growth of the damage in order to derive a more accurate model.

5.6 Residual Strength

The results of the residual strength tests were shown in Section 4.3.3. No conclusive results could be drawn from the experimental data. In general, notched cross-ply composite laminates have a rising tensile residual stress curve as the number of fa-

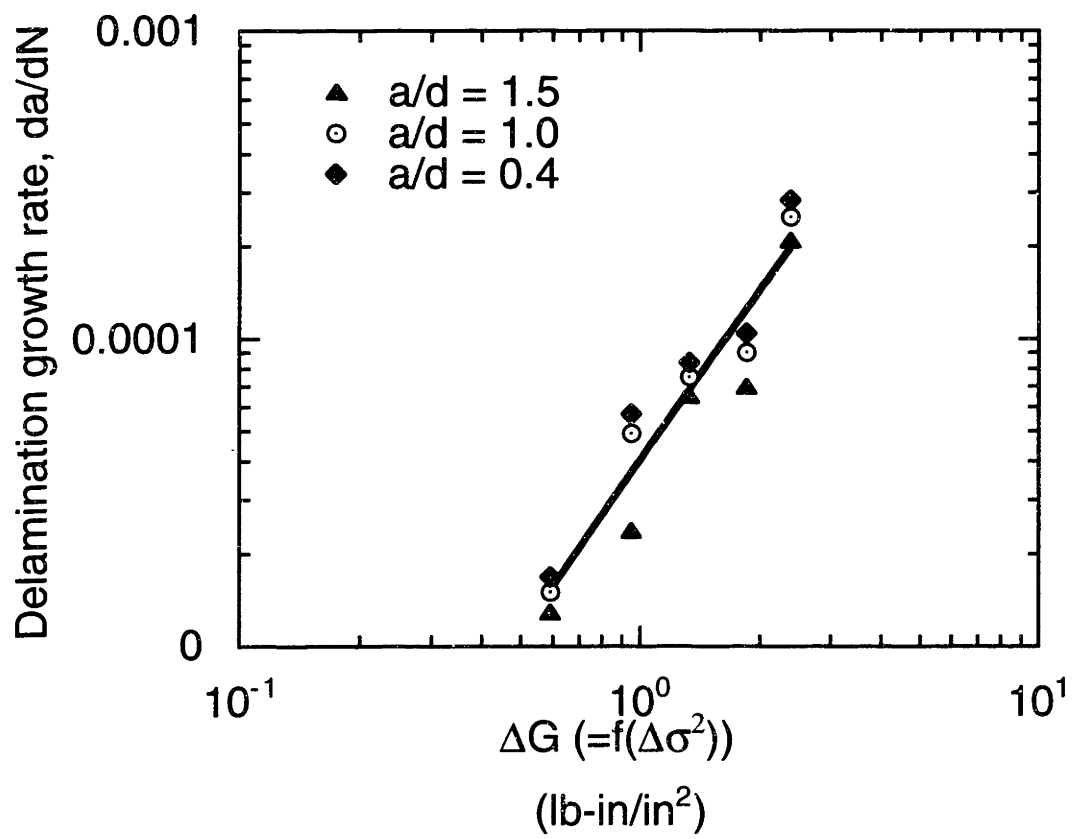


Figure 5-13: Damage growth rate as a function of stress level

tigue cycles increases (i.e. the residual stress increases as with increasing fatigue cycles) [21, 40]. The rise is attributed to the damage (ply splits, matrix cracks, delamination, etc.) that accumulates at the notch tip. The damage acts to blunt out the stress concentration due to the sharp notch and hence increase the strength of the specimen. In TiGr laminates, two competing mechanisms may be affecting the strength and at least partially nullifying one another. One effect is the blunting of the notch tip due to damage typically present in composites. The other is the loss of integrity in the facesheets, which can lead to higher stress in the PMC core and lower residual strength. One inconsistency that should be mentioned is that the initial fatigue tests at 60% OHT resulted in specimen fracture, which does not correlate with the hypothesis that the fibers are not damaged during fatigue. Other unobserved damage types, e.g. micro-buckling may be the cause of the inconsistency.

5.7 Design Implications

One of the goals of the project was to investigate the design implications of fatigue damage. This section describes how changing the lay-up of the laminate will affect the stress concentration and the delamination strain energy release rate.

5.7.1 Stress concentration factor

The stress concentration in an anisotropic material is a function of two parameters as defined in Equation 5.11 and Equation 5.12. Equation 5.13 is the formula for the maximum stress concentration for an anisotropic plate with an elliptical hole[43].

$$\lambda = \frac{E_1}{E_2} \quad (5.11)$$

$$\rho = \frac{(E_1 * E_2)^{\frac{1}{2}}}{2 * G_{12}} - (\nu_{12}\nu_{21})^{\frac{1}{2}} \quad (5.12)$$

Table 5.2: Stress concentration for alternate laminates

Lay-up	Stress concentration factor (σ/σ_∞)
[Ti/0/90/0 ₂] _s	4.6
[Ti/ \pm 15/90/0/] _s	4.1
[Ti/ \pm 30/90/0/] _s	3.3
[Ti/90/0 ₃ /Ti/0 ₃ /90/Ti] _t	4.3

$$\frac{\sigma}{\sigma_\infty} = 1 + \sqrt{2(1 + \rho)} * \lambda^{\frac{1}{4}} * \frac{b}{c} \quad (5.13)$$

where:

E_1 = Longitudinal Young's Modulus

E_2 = Transverse Young's Modulus

G_{12} = Shear Modulus

ν_{12}, ν_{21} = Poisson's Ratio

b, c = major and minor axes of elliptical hole

($\frac{b}{c} = 1$ for a circular hole)

For an isotropic material both λ and ρ are equal to 1, and the stress concentration factor is 3. One approach to lowering the stress concentration in TiGr laminates is to alter the lay-up and bring λ and ρ closer to 1, i.e. "more isotropic". Lowering the stress concentration around the hole could delay the onset and propagation of facesheet cracks, which in turn should delay the onset of facesheet delamination.

Three alternate lay-ups were investigated, two with $\pm \theta$ angle plies replacing 0° plies and one with an added titanium ply in the middle of the laminate. The laminate properties for each of the lay-ups were calculated using Classical Laminated Plate Theory. The results of the study are presented as Table 5.2.

The stress concentration decreases as the angle of the $\pm \theta$ plies is increased because the transverse modulus and the longitudinal modulus are closer together ($\lambda \rightarrow 1$). However, the angle plies also lower the ultimate strength and the stiffness of the

laminate. In design, trade-offs with other material requirements would be needed in order to optimize the angle.

5.7.2 Strain energy release rate

The SERR is also affected by the lay-up of the laminate. As explained in Section 5.3, a small decrease in SERR can lower the delamination growth rate by a much larger amount. Figure 5-14 shows the non-dimensional strain energy release rate plotted as a function of the ratio of facesheet thickness to PMC core thickness for the alternate lay-ups discussed above.

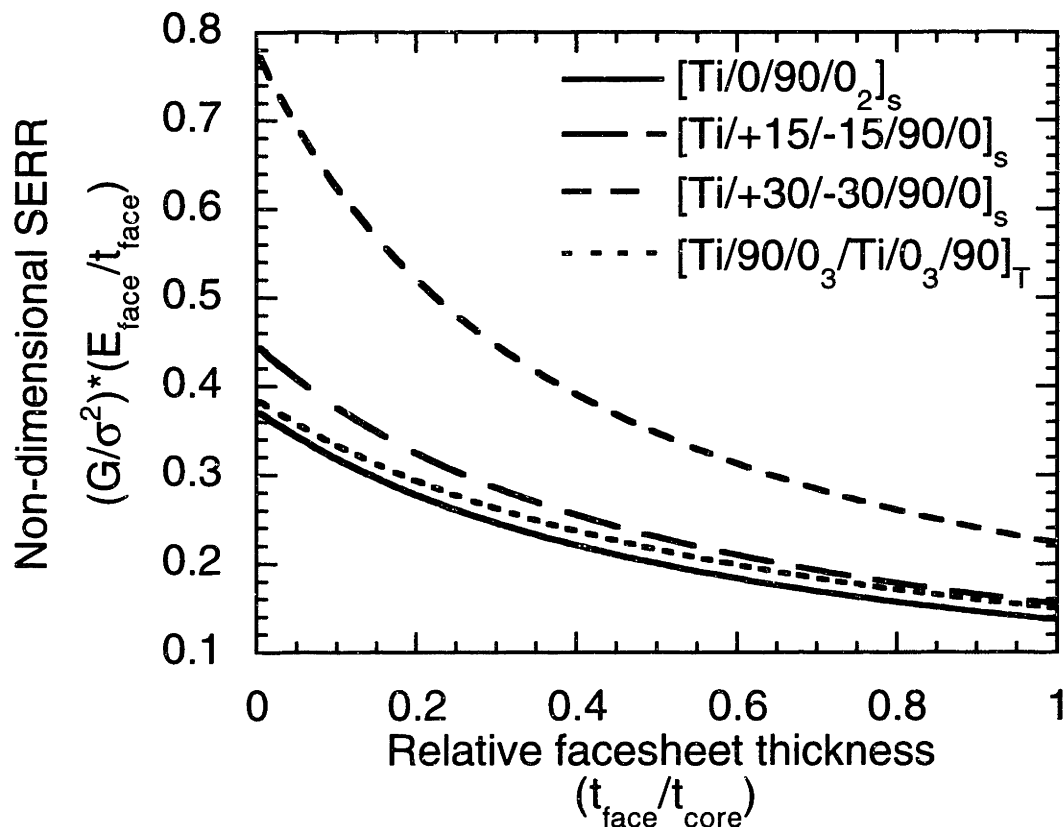


Figure 5-14: SERR for alternative lay-ups as a function of normalized facesheet thickness

The analysis shows that adding angle plies to the lay-up increases the delamination strain energy release rate significantly. In terms of delamination growth,

this is undesirable, however as shown in Section 5.7.1, the angle plies decrease the stress concentration. Design trade-offs would need to be conducted to determine the optimum configuration.

Chapter 6

Conclusions

6.1 Project Summary

The main focus of this project has been to develop the test procedures and to conduct elevated temperature, tension-compression fatigue tests on TiGr laminates containing open holes and to characterize and analyze the failure modes of the laminates.

A series of tests were performed at a range of stress levels to determine the number of cycles to failure. S-N plots were constructed from the test results, using 50% stiffness reduction as the arbitrary failure point. The S-N behavior using this failure metric was consistent over the range of cyclic loads applied.

The stiffness reduction as a function of fatigue cycles was recorded. Stiffness loss was shown to be a useful indication of the laminate damage state. The stiffness reduction was modeled and delamination was found to be the principal cause of stiffness loss.

Residual tensile strength tests were performed on some of the specimens after fatigue cycling. There was no systematic variation in strength and no obvious correlation between residual strength and stiffness loss.

A series of fatigue tests was performed to characterize damage progression prior to fatigue failure. A qualitative description of the damage progression and damage types was determined. First order analysis of the three principal damage mecha-

nisms, facesheet cracking, facesheet delamination, and ply splits, was performed. The facesheet cracks were consistent with fatigue crack initiation in monolithic titanium under similar stress states, the tendency to delaminate was consistent with the high strain energy release rate present in the laminate, and the 0° ply split growth rates were similar to those observed in $0^\circ/90^\circ$ cross-ply PMC laminates at similar stress levels.

6.2 Recommendations for Future Study

Further research and material development is required before TiGr can be used in structural applications. The research described herein has identified several areas requiring further investigation:

- Test wider specimens and monitor crack growth to determine if facesheet crack growth rate decreases.
- Test alternate PMC lay-ups to determine the effect on crack initiation, crack growth rate, and facesheet delamination
- Study the effect of transverse and longitudinal seams in specimens in terms of their interaction with facesheet cracks and the implications on delamination. These tests can also be used to study delamination rates and determine the toughness of the bond between the facesheet and the PMC core.
- Further investigation into the effects of temperature on the fatigue life and damage propagation.
- Load ratio effect on the damage mechanisms, to determine if the compression portion of the load cycle introduced further damage, and if it is responsible for fatigue failures.
- Finite element modeling of the damage to predict propagation patterns and stiffness loss.
- Impact testing of TiGr panels to determine damage state and residual strength after impact.

References

- [1] Bucci, R. J., L. N. Mueller, L. B. Vogelesang, and J. W. Gunnink, "ARALL Laminates," *Aluminum Alloys—Contemporary Research and Applications*, Vol. 31, 1989, pp. 295–322.
- [2] Gunnink, J. W., "Design Studies of Primary Aircraft Structures in ARALL Laminates," *Journal of Aircraft*, November 1988, pp. 1023–1032.
- [3] Wilson, C. D. and D. A. Wilson, "Effective Crack Lengths by Compliance Measurement for ARALL-2 Laminates," *Composite Materials: Fatigue and Fracture*, 1991, pp. 791–805. ASTM STP 1110.
- [4] Ritchie, R. O., W. Yu, and R. J. Bucci, "Fatigue Crack Propagation in ARALL Laminates: Measurement of the Effect of Crack-Tip Shielding From Crack Bridging," *Engineering Fracture Mechanics*, Vol. 32, No. 3, 1989, pp. 361–377.
- [5] Toi, Y. and Y. Fujiwara, "Fatigue Characterization of Fiber/Metal Laminates," in *1st AIAA Aircraft Engineering, Technology, and Operations Congress*, 1995. AIAA-95-3932.
- [6] Salivar, G. C. and C. A. Gardini, "The Influence of Stress Ratio and Temperature on the Fatigue Crack Growth Rate Behaviour of ARALL," *Journal of Composites Technology & Research*, Vol. 15, No. 1, 1993, pp. 46–51.
- [7] Osiroff, R., W. W. Stinchcomb, and K. L. Reifsnider, "Damage and Performance Characterization of ARALL Laminates Subjected to Tensile Cyclic Loading,"

- Composite Materials: Fracture and Fatigue*, 1991, pp. 772–790. ASTM STP 1110.
- [8] Papakyriacou, M., S. E. Stanzl-Tschegg, and J. Schijve, “Fatigue Behaviour of Notched Components of Fiber-Metal Laminates (GLARE),” in *Fatigue Design 1995*, Vol. 1, 1995, pp. 309–320.
 - [9] Roebroeks, G., “Fiber Metal Laminates: Recent Developments and Applications,” *International Journal of Fatigue*, 1994, pp. 33–42.
 - [10] Bertheau, D., N. Ranganathan, and J. Petit, “Estimation of Fiber Bridging Effect in ARALL 3 Laminate,” in *Fatigue 93*, Vol. II, Engineering Materials Advisory Services Ltd., 1993, pp. 1103–1108.
 - [11] Lee, T. C. and D. A. Wilson, “An Investigation of the Effects of Temperature on the Impact Behaviour and Residual Tensile Strength of an ARamid Aluminum Laminate (ARALL-2 Laminate,” *Composite Materials: Fatigue and Fracture*, 1991, pp. 806–821. ASTM STP 1110.
 - [12] Sun, C. T., A. Dicken, and H. F. Wu, “Characterization of Impact Damage in ARALL Laminates,” *Composites Science and Technology*, 1993, pp. 139–144.
 - [13] Hashagen, F., J. C. J. Schellekens, and R. de Borst, “Finite element procedure for modelling fibre metal laminates,” *Composite Structures*, Vol. 32, 1995, pp. 225–264.
 - [14] Marissen, R., *Fatigue crack growth in ARALL, A hybrid aluminium-aramid composite material: Crack growth mechanisms and quantitative predictions of the crack growth rates*, Ph.D. thesis, Delft University of Technology, 1984.
 - [15] Pettit, R. G., “Damage Tolerance Philosophy for Fiber/Metal Laminates,” in *SAE Technical Paper Series*, 1991.

- [16] Miller, J. L., D. J. Progar, W. S. Johnson, and T. L. S. Clair, "Preliminary Evaluation of Hybrid Titanium Composite Laminates," technical memorandum, NASA Langley Research Center, April 1994.
- [17] Li, E. and W. S. Johnson, "An Evaluation of Hybrid Titanium Composite Laminates for Room Temperature Fatigue," in *The Tenth International Conference on Composite Materials*, 1996.
- [18] Li, E., W. S. Johnson, and J. L. Miller, "High Temperature Hybrid Titanium Composite Laminates: An Early Analytical Assessment," in *The Tenth International Conference on Composite Materials*, 1995.
- [19] Fuchs, H. O. and R. I. Stephens, *Metal Fatigue in Engineering*, John Wiley & Sons, 1980.
- [20] Suresh, S., *Fatigue of Materials*, Cambridge University Press, 1991.
- [21] Bakis, C. E. and W. W. Stinchcomb, "Response of thick, notched laminates subjected to tension-compression cyclic loads," *Composite materials: Fatigue and fracture*, 1986, pp. 314–334. ASTM STP 907.
- [22] Spearing, S. . and P. W. R. Beaumont, "Fatigue damage mechanics of composite materials. I: Experimental measurement of damage and post-fatigue properties," *Composites Science and Technology*, Vol. 44, 1992, pp. 159–168.
- [23] Spearing, S. M., P. W. R. Beaumont, and M. F. Ashby, "Fatigue damage mechanics of composite materials. II: A damage growth model," *Composites Science and Technology*, Vol. 44, 1992, pp. 169–177.
- [24] Spearing, S. M. and P. W. R. Beaumont, "Fatigue damage mechanics of composite materials. III: Prediction of post-fatigue strength," *Composites Science and Technology*, Vol. 44, 1992, pp. 299–307.
- [25] O'Brien, T. K., "Characterization of delamination onset and growth in a composite laminate," *ASTM STP 775*, 1982, pp. 140–167.

- [26] Bruce R. Trethewey, J., J. John W. Gillespie, and L. A. Carlsson, "Mode II Cyclic Delamination Growth," *Journal of Composite Materials*, Vol. 22, May 1988, pp. 459–483.
- [27] Dahlen, C. and G. S. Springer, "Delamination Growth in Composites Under Cyclic Loads," *Journal of Composite Materials*, Vol. 28, No. 8, 1994, pp. 732–781.
- [28] Fanning, J. C., "TIMETAL 15-3 Property Data," in *Beta Titanium Alloys in the 1990's* (Eylon, D., R. Boyer, and D. Koss, eds.), The Minerals, Metals & Materials Society, 1993.
- [29] Hartness, J. T., "The characterization of a thermoplastic polyimide composite," in *Technology Transfer in a Global Community*, Society for the Advancement of Material and Process Engineering, 1996.
- [30] Li, E., "The Boeing Company," 1996. Personal Communication.
- [31] Fisher, J. M., A. N. Palazotto, and R. S. Sandhu, "A Study of Failure Characteristics in Thermoplastic Composite Material at 250°F (121°C)," *The Journal of Composite Technology and Research*, Vol. 13 1991, pp. 152–160.
- [32] Kortschot, M. T. and P. W. R. Beaumont, "Damage mechanics of composite materials. I—Measurement of damage and strength," *Composites Science and Technology*, Vol. 39, No. 4, 1990, pp. 289–301, 303–326.
- [33] Kortschot, M. T., P. W. R. Beaumont, and M. F. Ashby, "Damage mechanics of composite materials. III—Prediction of damage growth and notched strength," *Composites Science and Technology*, Vol. 40, No. 2, 1990, pp. 147–165.
- [34] Kortschot, M. T. and P. W. R. Beaumont, "Damage mechanics of composite materials. IV—The effect of lay-up on damage growth and notched strength," *Composites Science and Technology*, Vol. 40, No. 2, 1990, pp. 167–179.

- [35] Wang, S. S., J. F. Mandell, and F. F. McGarry, "Three Dimensional Solution for a Through-Thickness Crack in a Cross-Plied Laminate," *ASTM STP 593*, 1975a, pp. 36–60.
- [36] Wang, S. S., J. F. Mandell, and F. F. McGarry, "Three Dimensional Solution for a Through-Thickness Crack in a Cross-Plied Laminate," *ASTM STP 593*, 1975b, pp. 61–85.
- [37] Young, W. C., *Roark's Formula's for Stress and Strain*, McGraw-Hill, Inc., sixth ed., 1989.
- [38] Bishop, S. M., "Stresses Near an Elliptical Hole in an Orthotropic Sheet," Tech. Rep. 72026, Royal Aircraft Establishment, 1972.
- [39] Fanning, J. C., "Fatigue Data for *TIMETAL* 15-3," in *Beta Titanium Alloys in the 1990's* (Eylon, D., R. Boyer, and D. Koss, eds.), The Minerals, Metals & Materials Society, 1993.
- [40] Spearing, S. ., P. W. R. Beaumont, and M. T. Kortschot, "The fatigue damage mechanics of notched carbon fibre/PEEK laminates," *Composites*, Vol. 23, No. 5, September 1992.
- [41] Ashby, M. F., K. E. Easterling, R. Harrysson, and S. K. Maiti, "The Fracture and Toughness of Woods," in *Proceedings of the Royal Society, London*, 1985, pp. 261–280.
- [42] William D. Callister, J., *Material Science and Engineering: An Introduction*, John Wiley & Sons, Inc., 1997.
- [43] Suo, Z., G. Bao, B. Fan, and T. C. Wang, "Orthotropy Rescaling and Implications for Fracture in Composites," *International Journal of Solids and Structures*, Vol. 28, No. 2, 1991, p. 235.

Appendix A

A.1 Stress Concentration Code

Anisotropic

```
clear;
```

```
%%%%%%%%%%  
% The Y dir is the fiber direction and the loading direction  
%%%%%%%%%
```

```
%Material properties of the different lay-ups
```

```
%TiGr 2-6-2  
Ey = 17.7e6; %psi  
Ex = 8.8e6; %psi  
NUxy = .162;  
Gxy = 1.66e6; %psi
```

10

```
%TiGr [Ti/+15/-15/90/0]s  
%Ey = 16.3e6; %psi  
%Ex = 8.75e6; %psi  
%NUxy = .221;  
%Gxy = 2.2e6; %psi
```

20

```
%TiGr [Ti/+30/-30/90/0]s  
%Ey = 13.e6; %psi  
%Ex = 8.92e6; %psi  
%NUxy = .32;  
%Gxy = 3.28e6; %psi
```

```
%TiGr [Ti/90/0_3/Ti/0_3/90/Ti]t  
%Ey = 17.5e6; %psi  
%Ex = 9.56e6; %psi  
%NUxy = .19;  
%Gxy = 2.03e6; %psi
```

30

```
%Computation from Bishop, Sarah M. "Stresses Near an Elliptical Hole in an
```

```

%Orthotropic Sheet"

p = Ey/(2*Gxy) - NUxy;
q = Ey/Ex;

beta1 = sqrt((p/q)*(1 + sqrt(1-q/p^2)));
beta2 = sqrt((p/q)*(1 - sqrt(1-q/p^2)));

%Limiting condition of round hole
a = .125;
b = .125;
rho = b^2/a;
eps = b/a;

x = [0:.005:.25];
y = [0:.005:.25];

%Loop through x and y axes
for j = 1:length(x)
    for k = 1: length(y)
        Z1(j,k) = x(j)/a + i.*beta1.*y(k)/a;
        Z2(j,k) = x(j)/a + i.*beta2.*y(k)/a;
        phi1(j,k) = sqrt(Z1(j,k)^2 - 1 + eps^2*beta1^2);
        phi2(j,k) = sqrt(Z2(j,k)^2 - 1 + eps^2*beta2^2);

        %set up conditional statement to set stress concentration to 0 when
        % x and y coordinates are in the circle region

        if ((x(j)^2/a^2 + y(k)^2/b^2) < 1)
            sigma_y_norm(j,k) = 0.01;
            sigma_x_norm(j,k) = 0;
            sigma_xy_norm(j,k) = 0;
        else
            sigma_y_norm(j,k) = 1 + real(((1/(beta1-beta2))*((beta2/(1-eps*beta1))*
                (1-Z1(j,k)/phi1(j,k)) - (beta1/(1-eps*beta2))*
                (1-Z2(j,k)/phi2(j,k)))));

            sigma_x_norm(j,k) = -real((beta1*beta2/(beta1-beta2))*
                ((beta1/(1-eps*beta1))*(1-Z1(j,k)/phi1(j,k)) -
                (beta2/(1-eps*beta2))*(1-Z2(j,k)/phi2(j,k)))));

            sigma_xy_norm(j,k) = imag((beta1*beta2/(beta1-beta2))*
                ((beta1/(1-eps*beta1))*(1-Z1(j,k)/phi1(j,k)) -
                (beta2/(1-eps*beta2))*(1-Z2(j,k)/phi2(j,k)))));
        end
    end
end

%Plot results
surf(x,y,sigma_y_norm)
axis([0,.25,0,.25,0,5])
xlabel('Longintudinal Position (in)')
ylabel('Transverse Position (in)')

```

```
zlabel('Stress Concentration Factor')
```

Isotropic

```
clear;
```

```
%%%%%%%%%%
```

```
% The Y dir is the fiber direction and the loading direction
```

```
%%%%%%%%%%
```

```
%Computation from Bishop, Sarah M. "Stresses Near an Elliptical Hole in an  
%Orthotropic Sheet"
```

```
beta1 = 1;
```

```
beta2 = 1;
```

10

```
%Limiting condition of round hole
```

```
a = .125;
```

```
b = .125;
```

```
rho = b^2/a;
```

```
eps = b/a;
```

```
x = [0:.005:.25];
```

```
y = [0:.005:.25];
```

20

```
for j = 1:length(x)
```

```
    for k = 1: length(y)
```

```
        Z(j,k) = x(j)/a + i*y(k)/a;
```

```
%set up conditional statement to set stress concentration to 0 when
```

```
% x and y coordinates are in the circle region
```

```
if ((x(j)^2/a^2 + y(k)^2/b^2) < 1)
```

```
    sigma_y_norm(j,k) = 0.01;
```

```
    sigma_x_norm(j,k) = 0;
```

```
    sigma_xy_norm(j,k) = 0;
```

30

```
else
```

```
    sigma_y_norm(j,k) = 1 + real(1/(2*Z(j,k)^2)+3/(2*Z(j,k)^4)+(2*i*y(k))/  
        (a*Z(j,k)^3));
```

```
    sigma_x_norm(j,k) = real(3/(2*Z(j,k)^2)-3/(2*Z(j,k)^4)-(2*i*y(k))/  
        (a*Z(j,k)^3));
```

```
    sigma_xy_norm(j,k) = imag(-1/(2*Z(j,k)^2)+3/(2*Z(j,k)^4)+(2*i*y(k))/  
        (a*Z(j,k)^3));
```

```
end
```

```
end
```

40

```
end
```

```
surf(x,y,sigma_y_norm)
```

```
axis([0,.25,0,.25,0,5])
```

```
xlabel('Longitudinal Position (in)')
```

```
ylabel('Transverse Position (in)')
```

```
zlabel('Stress Concentration Factor')
```

A.2 Strain Energy Release Rate Code

```
clear;
%material properties.

%E_Ti = 15.5, Al = 10, Quasi = 8.7, 90, 1.3
EL = 15.5e6;
ET = 16.3e6;
nuLT = .33;
GLT = 6e6;

EL_PMC = 23.5e6;
ET_PMC = 1.e6;
nuLT_PMC = .35;
GLT_PMC = .65e6;

Q_Ti = getQ(EL,ET,nuLT,GLT);
Q_PMC = getQ(EL_PMC,ET_PMC,nuLT_PMC,GLT_PMC);

t = [0:.0002:.0432]; %vector of various face sheet thicknesses
t=.005;

%set facesheet thickness and angles
n_face = 2;
theta_face = [0,0];

%Define core ply thicknesses and orientation angles.
n_core = 8;

thick_core = [.0054,.0054,.0054,.0054,.0054,.0054,.0054,.0054];
theta_core = [0,90,0,0,0,0,90,0];

%different angle lists of the different lay-ups

%theta_core = [15,-15,90,0,0,90,-15,15];
%theta_core = [30,-30,90,0,0,90,-30,30];

%extra Ti ply setup
%theta_core = [90,0,0,0,0,0,0,90];
%thick_core = [.0054,.0054,.0054,.0054,.0054,.0054,.0054,.0054];

t_core = sum(thick_core); %total core thickness

%specimen width
W = 1.5;

%applied load
P =3600;

Qmat_face =[Q_Ti,Q_Ti];
```

```

%Get laminate properties of core
for i = 1:n_core
    Qmat_core=[Qmat_core;rotateQ(Q_PMC,theta_core(i))];
end

%Sets properties of lay-up with extra Ti ply (unsymmetric)
%Qmat_core=[rotateQ(Q_PMC,90);
%rotateQ(Q_PMC,0);
%rotateQ(Q_PMC,0);
%rotateQ(Q_PMC,0);
%rotateQ(Q_Ti,0);
%rotateQ(Q_PMC,0);
%rotateQ(Q_PMC,0);
%rotateQ(Q_PMC,0);
%rotateQ(Q_PMC,90)]

A_core = getA(n_core,Qmat_core,thick_core);
a_core = inv(A_core);
E_core = 1/(a_core(1,1)*t_core);

for j= 1:(length(t))

    t_face = 2*t(j);          %total face sheet thickness(both sides)
    E_face = EL; %Face sheet modulus is longitudinal modulus of titanium

%in undamaged portion, the load is divided between the face sheets and the
%core based on modulus
P_core = P./(1+ (W.*t_face.*E_face)./(W.*t_core.*E_core));
P_face = P./(1+ (W.*t_core.*E_core)./(W.*t_face.*E_face));

%calculate stress levels
sigma_face = P_face./(W.*t_face);
sigma_core = P_core./(W.*t_core);
sigma = P./(W.*(t_core));

%calculate energy levels
dU1 = (.5/E_core).*sigma.^2.*(t_core);
dU2 = ((.5/E_face).*sigma_facc.^2.*(t_face)+(.5/E_core).*sigma_core.^2.*(t_core));
dU(j) = dU1-dU2

%set up non-dimensional results
Y(j) = dU(j).*E_face./(sigma.^2.*t_face);
X(j) = t(j)/t_core;
end

```

A.3 Stiffness Loss Code

Titanium cracks

clear

```

%Damage Length
d=[0:.1:4.5];

%Material Properties
W = 1.5;
t_face = .005;
E_lam = 17.7e6;
t_ply = .0054;
E_core = 18e6;

%Area calculation
A1 = (2*t_face+8*t_ply)*W;
A2 = 8*t_ply*W;

%Critical length
ext = 25/25.4;

%Initial stiffness
K0 = E_lam*A1/(2*ext);

%Loop over damage length
for i = 1:(length(d))
    %set critical length
    L1(i) = (ext-d(i));
    %set stiffnesses
    K1 = A1*E_lam/L1(i);
    K2 = A2*E_core/(2*d(i));

    %Check when damage is past extensometer gauge length
    if d(i) <= ext
        Ktot(i) = 1/(2/K1+ 1/K2);
    else
        Ktot(i) = K2;
    end
end

%normalize stiffness
Ktot = Ktot./K0;
d = d./ext;

```

10

20

30

40

90° ply loss

```

clear

%Material properties
EL = 15.5e6;
ET = 16.3e6;
nuLT = .33;
GLT = 6e6;

EL_PMC = 23.5e6;

```

```

ET_PMC = 1e6;
nuLT_PMC = .35;
GLT_PMC = .65e6;

%Use CLPT to get core properties
Q_Ti = getQ(EL,ET,nuLT,GLT);
Q_PMC = getQ(EL_PMC,ET_PMC,nuLT_PMC,GLT_PMC);

thick1 = [.005,.0054];
thick2 = [.0054,.0054,.0054,.0054];
h1 = sum(thick1);
h2 = sum(thick2);

theta = [0,0];
Qmat1 = [Q_Ti,Q_PMC];
Qmat2 = [Q_PMC,Q_PMC,Q_PMC,Q_PMC];

%properties of outer 2 layers
A1 = getA(2,Qmat1,thick1);
a1 = inv(A1);
E1 = 1/(a1(1,1)*h1);

%properties of middle 4 layers
A2 = getA(4,Qmat2,thick2);
a2 = inv(A2);
E2 = 1/(a2(1,1)*h2);

%Damage length
d=[0:.1:4.5];

%material propeties of undamaged section
W = 1.5;
E_lam = 17.7e6;
t_ply = .0054;

A_lam = (2*.005+8*t_ply)*W;
A_outer = h1*W;
A_inner = h2*W;

%Critical length
ext = 25/25.4;

%initial stiffness
K0 = E_lam*A_lam/(2*ext);

%Loop over damage length
for i = 1:(length(d))
    %set critical length
    L1(i) = (ext-d(i));
    %set stiffnesses
    K1 = A_lam*E_lam/L1(i);
    K2 = 2*A_outer*E1/(2*d(i))+ A_inner*E2/(2*d(i));

```



```

%Check when damage is past extensometer gauge length
if d(i) <= ext
    Ktot(i) = 1/(2/K1+ 1/K2);
else
    Ktot(i) = K2;
end
end

%normalize stiffness
Ktot = Ktot./K0;
d = d./ext;

```

70

Combined damage

```

clear

%Material properties
EL = 15.5e6;
ET = 16.3e6;
nuLT = .33;
GLT = 6e6;

EL_PMC = 23.5e6;
ET_PMC = 1e6;
nuLT_PMC = .35;
GLT_PMC = .65e6;

%Use CLPT to get core properties
Q_Ti = getQ(EL,ET,nuLT,GLT);
Q_PMC = getQ(EL_PMC,ET_PMC,nuLT_PMC,GLT_PMC);

thick1 = [.0054];
thick2 = [.0054,.0054,.0054,.0054];
h1 = sum(thick1);
h2 = sum(thick2);

theta = [0];
Qmat1 = [Q_PMC];
Qmat2 = [Q_PMC;Q_PMC;Q_PMC;Q_PMC];

%properties of outer 2 layers
A1 = getA(1,Qmat1,thick1);
a1 = inv(A1);
E1 = 1/(a1(1,1)*h1)

%properties of middle 4 layers

```

10

20

30

```

A2 = getA(4,Qmat2,thick2);
a2 = inv(A2);
E2 = 1/(a2(1,1)*h2\

```

```

%Damage length
d=[0:.1:4.5];

```

```

%material propeties of undamaged section
W = 1.5;
E_lam = 17.7e6;
t_ply = .0054;

```

```

A_lam = (2*.005+8*t_ply)*W;
A_outer = h1*W;
A_inner = h2*W;

```

```

%Critical length
ext = 25/25.4;

```

```

%initial stiffness
K0 = E_lam*A_lam/(2*ext);

```

```

%Loop over damage length
for i = 1:(length(d))
    %set critical length
    L1(i) = (ext-d(i));
    %set stiffnesses
    K1 = A_lam*E_lam/L1(i);
    K2 = 2*A_outer*E1/(2*d(i))+ A_inner*E2/(2*d(i));

```

```

%Check when damage is past extensometer gauge length
if d(i) <= ext
    Ktot(i) = 1/(2/K1+ 1/K2);
else
    Ktot(i) = K2;
end
end

```

```

%normalize stiffness
Ktot = Ktot./K0;
d = d./ext;

```

40

50

60

70

THESIS PROCESSING SLIP

FIXED FIELD ill _____ name _____

index _____ biblio _____

► COPIES Archives Aero Dewey Eng Hum

Lindgren Music Rotch Science

TITLE VARIES ► ☐ _____

NAME VARIES ► ☐ _____

IMPRINT (COPYRIGHT) _____

► COLLATION 1072 _____

► ADD DEGREE _____ ► DEPT. _____

SUPERVISORS _____

NOTES

cat'r

date

► DEPT Aero

page
► F44

► YEAR 1998 ► DEGREE M.S.

► NAME BURIANEK, Dennis Arthur